Improving drug discovery using image-based multiparametric analysis of epigenetic landscape.

Chen Farhy[1], Luis Orozco[1], Fu-Yue Zeng[1], Ian Pass[1], Jarkko Ylanko[2], Santosh Hariharan[2], Chun-Teng Huang[1], David Andrews[2,3], and Alexey V. Terskikh[1*].

[1]Sanford Burnham Prebys Medical Discovery Institute, La Jolla, California, USA

[2]Biological Sciences Platform, Sunnybrook Research Institute.

[3]Departments of Biochemistry and Medical Biophysics, University of Toronto, Ontario, Canada.

*Correspondence should be addressed to A.V.T. (terskikh@sbpdiscovery.org).

Abstract

With the advent of automatic cell imaging and machine learning, high-content phenotypic screening has become the approach of choice for drug discovery due to its ability to extract drug specific multi-layered data and compare it to known profiles. In the field of epigenetics such screening approaches has suffered from the lack of tools sensitive to selective epigenetic perturbations. Here we describe a novel approach Microscopic Imaging of Epigenetic Landscapes (MIEL) that captures patterns of nuclear staining of epigenetic marks (e.g. acetylated and methylated histones) and employs machine learning to accurately distinguish between such patterns (1). We demonstrated that MIEL has superior resolution compared to conventional intensity thresholding techniques and enables efficient detection of epigenetically active compounds, function-based classification, flagging possible off-target effects and even predict novel drug function. We validated MIEL platform across multiple cells lines and using dose-response curves to insure the robustness of this approach for the high content high throughput drug discovery.

Introduction

Posttranscriptional modifications of histone ‘tails’ modulate local chromatin and constitutes the physical basis for transcription regulation (2, 3). Enzymes producing these modifications (epigenetic writers and erasers) as well as chromatin-associated proteins which read the modifications (epigenetic readers) have been associated with initiation and progression of multiple cancer types (4). Several drugs inhibiting such epigenetic targets have recently been approved for clinical use and many more are currently in clinical trials (4-6). This, together with the possible applicability of epigenetic drugs in other diseases including neurological and cardiovascular disorders make these an attractive target for drug discovery (7-9). Continuing the trend set in the post-Human Genome Project era, much of the effort exerted toward developing new epigenetic drugs has been directed towards target-based drug discovery, leading to a proliferation of both biochemical and cell-based assays (10, 11).Initial screening for epigenetic drugs is often done by acellular biochemical assays. Though these provide valuable

information regarding specificity, they employ purified (often truncated) enzymes and isolated histone substrates (or even short peptides) (11-14). However, many epigenetic targets function as part of protein complexes and therefore may be misrepresented by such synthetic systems (15, 16). In addition, adjacent histone modification could potentially affect the function of assayed enzymes (17, 18).The most commonly used cellular alternatives are lysis and ELISA based assays, such as AlphaLISA (PerkinElmer). These circumvent many of these limitations and provide additional information such as estimation of toxicity and cell permeability but yield the ability to test direct enzymatic activity (10, 11, 14, 19).Over the last decades the low cost and scalability of high content screening approaches have greatly increased its prevalence for drug discovery. More recently, the addition of novel image analysis tools coupled with multiparametric analysis and machine learning have had a significant impact on our ability to understand and process the output of phenotypic screening (20, 21). Despite these advantages, such assays are not currently adapted and optimized for epigenetic drug discovery.

Here we demonstrate the ability of MIEL, a high content screening approach for profiling the endogenous patterns of histone modifications and chromatin organization, to detected active epigenetic compounds and classify them by their molecular function. Given its malignancy, the poor therapeutic benefits of current treatments and the proclivity of epigenetic events in development and progression of glioblastoma (4, 22-24), we chose patient derived glioblastoma lines to evaluate the advantages of MIEL-based phenotypic screening approach.

Results

The MIEL platform.

We have developed a novel phenotypic screening platform, MIEL, which interrogates the epigenetic landscape at both population and single cell level using image derived features and machine learning (1). MIEL takes advantage of epigenetic marks such as histone methylation and acetylation, which are always present in eukaryotic nuclei and can be revealed by immunostaining. It analyzes the immunolabeling patterns of epigenetic marks using conventional image analysis methods for segmentation of nuclei, feature extraction and previously described machine learning algorithms (25) (Fig. 1a and Methods). Primarily, we utilized 4 histone modifications: H3K27me3 and H3K9me3, which are associated with condensed (closed) facultative and constitutive heterochromatin, respectively; H3K27ac, associated with transcriptionally active (open) areas of chromatin, especially at promoter and enhancer regions; and H3K4me1, associated with enhancers and other chromatin regions (Fig. 1a; (26, 27)). To focus on the intrinsic pattern of epigenetic marks, we use only texture-associated features (eg, Haralick's texture features (28), threshold adjacency statistics, and radial features (29)) for multivariate analysis. Previous studies have successfully employed similar features for cell painting techniques combined with multivariate analyses to accurately classify subcellular localization of proteins (29),

cellular subpopulations (30), and drug mechanisms of action (25, 31-33). One of key advantages of MIEL is the very phenotypic traits used for deriving texture features – the representation of epigenetic landscapes within the single nuclei (1).

MIEL naturally lends itself to screening of epigenetic drugs. We put to test the fine resolution of the MIEL approach by screening a library of 222 epigenetically active compounds many with known targets among epigenetic writers, erasers, or readers (SBP epigenetic library, Supplementary Fig. 1a,b). Our analysis was focused on the accuracy of detection and ranking of active drugs, our ability to predict drug function (off target effect), robustness across cell lines and the dose-response, and, finally, the utility of MIEL to inform about the mechanism of drug action.

MIEL markedly improves detection of epigenetically active drugs

Current phenotypic methods employed to screen for the drugs targeting epigenetic enzymes rely on staining for the relevant histone modification and monitoring changes in average fluorescent intensity (34, 35). To test the ability of the MIEL approach to detect active compounds and compare it to intensity based methods, GBM2 cells were treated with previously defined drugs targeting a wide range of functional targets (Supplementary Fig. 1a,b). Drugs were given in triplicates at 10uM for 24 hours and treated cells were stained for multiple histone modifications expected to exhibit alterations following drug treatment (H3K9me3, H3K27me3, H3K27ac and H3K4me1). Image analysis including nuclei segmentation and features extraction was conducted, as previously described (25) on Acapella 2.6 (PerkinElmer). Phenotypic profiles were generated for each compound and control (DMSO) wells. These are vectors composed of 1048 (262 features per modification X 4 modifications) texture features derived from the staining of each histone modification and represent the average value for each feature across all stained cells in each cell population (drug or DMSO). When treatment reduced cell count to under 50 imaged nuclei per well, compound was deemed toxic and excluded from analysis. Following feature normalization by z-score, Euclidean distance between vectors of compounds and DMSO treated cells were calculated. These distances were then normalized (z-score) to the average distance between DMSO replicates and standard deviation of these distances. Compounds with distance z-score of greater than 3 were defined as active (Fig. 1A; see Methods section). This analysis identified 122 compound which induced significant epigenetic changes. Active compounds were not uniformly distributed across all functional drug categories. Rather, we identified 10 categories in which 50% of the drugs were identified as active and nontoxic and 13 categories in which 25% or less of the drugs induced detectable epigenetic alterations following a 24-hour treatment (Fig. 1b). To compare MIEL with current thresholding methods we repeated the calculation using mean fluorescence intensity for all histone modifications. Mean intensity for each drug was normalized (z-score) against DMSO. This analysis identified 94 active compounds, for which z-scored intensity for at least one of the histone

modifications was greater than 3 or lower than -3. These were distributed across the functional categories similar to MIEL identified compounds (Fig. 1b).

To inspect the contribution of individual histone modifications we repeated both the MIEL and thresholding analyses for each of the 4 modifications individually. A single modification MIEL based analysis yielded similar detection rates to the combination of modifications across most functional categories (Supplementary Fig. 2a). Intensity based analysis using individual modifications yielded lower detection rates compared to the combination of modifications and displayed equal or reduced detection rates when compared to MIEL in all categories and modifications (Supplementary Fig. 2a). Of note, 3 of the 4 modifications used for MIEL analysis showed similar detection rates across most functional categories. However, the modification H3K27me3 consistently showed reduced detection rates over most active categories (Supplementary Fig. 2a) with the exception of EZH1/2 inhibitors, possibly due to the role of these enzymes in regulating this posttranslational modification. To further compare the MIEL and thresholding detection methods we estimated the magnitude of epigenetic alterations induced by active compounds. We calculated the fold increase in distance from DMSO (normalized to average distance between DMSO replicates) as well as the absolute fold change of fluorescence intensity for active compounds in each category. This analysis indicated increased effect size for MIEL based analysis in all categories tested (Supplementary Fig. 2b). Taken together, these results demonstrate that MIEL analysis markedly improves detection of epigenetically active compounds as compared to current image-based thresholding methods.

MIEL enables Identification of drug function and off-target effects detection

One of the key advantages of phenotypic profiling methods, like MIEL, is the ability to classify compounds by function and identify nonspecific effects through comparison with profiles of well-defined controls. To assess the ability of MIEL to correctly group compounds by function we applied discriminant to all active-non-toxic compounds from categories which had at least 4 such compounds (total 84 compounds over 7 categories in addition to 48 DMSO replicates). All 132 populations were used as training data for a quadratic discriminant analysis performed employing a stepwise model on all texture features derived from images of the four histone modification (features displaying multicollinearity were reduced) and the model was tested through cross validation by ‘leave one out’ (see method). This analysis demonstrates the ability of MIEL to separate multiple categories of epigenetically active drugs with an average accuracy of 86.7% (Fig. 1c,d). Although many of the epigenetically active compounds induced alterations in average fluorescence (Supplementary Fig. 3a), a discriminant analysis utilizing intensity measurements from all 4 channels was ineffective at separating the various categories and yielded only 45% average accuracy (Supplementary Fig. 3b). Of note, the compound library used in this study included Pan HDACi, Class I HDACi and Class I HDACi known to also target HDAC6. HDAC inhibitors targeting both Class I and HDAC 6 displayed same

profile as Pan HDAC and the two categories were undistinguishable through discriminant analysis. This is likely due to high expression of HDAC Class I and HDAC 6 and low expression of other HDACs in the GBM line (Supplementary Fig. 4a,b,c). To test whether individual histone modification textures contain sufficient information to distinguish between the various drug classes we performed discriminant analysis using features derived from each modification. This degraded MIEL's ability to separate compound subclasses affecting similar histone modification changes such as Class I and Pan HDAC inhibitors, but retained its ability to separate major categories, such as histone phosphorylation and deacetylation (Fig. 1e, Supplementary Fig. 3c).

Of the 84 compounds tested 7 (8.3%) were identified as active but miss classified by MIEL. One of these was Valproic acid, a commonly used anticonvulsant (36) also shown to function as a Pan HDAC inhibitor at high concentrations (37). Though Valproic acid is expected to inhibit HDACs only at high concentrations (>1.2mM), a short 24 hour treatment induced detectable epigenetic changes even at low concentrations (<30uM, Supplementary Fig. 5a). However, quantification of H3K27ac and H3K27me3 immunofluorescence intensity indicated that at these concentrations it did not increase histone acetylation or decreased histone methylation similar to other Pan HDAC inhibitors (TSA, SAHA; Supplementary Fig. 5b). To test, whether the observed epigenetic changes resulted in corresponding transcriptomic alterations we sequenced RNA from GBM2 cells treated with either DMSO, TSA, SAHA or Valproic acid (15uM) for 24 hours and identified all genes altered by at least one of the drugs (as compared to DMSO; 118 genes). This analysis demonstrated that the Pan HDAC inhibitors induced similar transcriptomic changes and that these were not reflected in the transcriptomic profile of Valproic acid treated cells (Supplementary Fig. 5c). To test whether MIEL profiles reflected global drug induced transcriptomic profiles, FPKM values for all expressed genes (FPKM>1 in at least one cell population) were used to calculate Euclidean distance between all 4 cell populations. FPKM-based distances were then correlated to image texture feature-based distances which yielded a high and significant correlation between these metrics ($R=0.91$, $pv<0.05$; Supplementary Fig. 5a). Taken together these results demonstrate the enhanced ability of the MIEL approach to identify epigenetically active compounds, accurately categories them according to their molecular function and detect off-target effects of tested compounds.

MIEL profiles are coherent across drug concentrations and cell lines

As drugs vary in potency, the ability to predict the function of unknown drugs relies on generating functional category specific profiles that remain valid over a range of activity levels. To test the ability of MIEL to correctly identify the functional category of drugs with different potency we treated GBM2 cells with drugs from several active categories at a range of concentrations (0.1, 0.3, 1, 3, 10uM) and conducted discriminant analysis aimed at separating the different concentrations in each class. We found that for most categories tested (Aurora-i, JAKi, SIRTi and EZH1/2i) the discriminant analysis

yielded low average accuracy of classification (32%, 25%, 35% and 55% respectively; Fig. 2a, Supplementary Fig. 6a) indicating similar MIEL profiles across all drug concentrations tested. However, Pan HDAC and HDAC Class I inhibitors displayed progressive profile changes allowing the discriminant analysis to separate the different concentrations at 77% and 78% accuracy (Fig. 2a, Supplementary Fig. 6a).

In addition to their on-target effect, drugs may induce epigenetic alterations through toxicity and stress. To estimate the impact of toxicity on drug induced profile changes and its contribution to drug miss-classification across a range of concentrations, we plotted z-scored distance from DMSO (effect size) against z-scored nuclei count (a proxy for cytotoxicity) for GBM2 cells treated at a range of drug concentrations (0.1, 0.3, 1, 3, 10uM). This demonstrated that some compound classes, such as Aurora and JAK inhibitors, induce epigenetic alterations only at concentrations at which cell count is significantly reduced, whether through toxicity or direct effect on proliferation (Fig. 2b); while other compounds, such as HDAC inhibitors, characteristically have a range of concentrations at which epigenetic alterations are not accompanied by reduced cell count (Fig. 2b). Interestingly, both SIRTi and EZH1/2 inhibitors affected significant epigenetic changes without inducing significant changes in cell count (Fig. 2b).

Testing candidate drugs in multiple cell lines can help to gauge their inclusivity and to identify tumor subtypes which do not respond to a specific drug or drug class. To test whether MIEL readouts are coherent across multiple glioblastoma TPCs we treated 4 cell lines with a subset of drugs from the epigenetic library (57 drugs), derived phenotypic profiles and calculated their effect size (z-scored Euclidean distance from DMSO replicates). This revealed a significant positive correlation between all 4 cell lines pointing to similarities in their drug sensitivity profiles and demonstrating the robustness of the MIEL read out (Fig. 2c,d). In addition, we found that the magnitude of effect for some drugs classes showed high correlation to the level of target gene expression. For example, SIRTi treatment was significantly more effective (n=4 compounds, $p<0.02$; Supplementary Fig. 6b,c) in lines showing reduced Sirt1 expression (the main SIRT to deacetylate histone 3; Supplementary Fig. 6b,c) and there was a high correlation between Sirt1 expression and effect size ($R=-0.87$; Supplementary Fig. 6c). These results point to the sensitivity of MIEL and to its ability to reflect internal differences between cell populations.

Due to inter- and inta- tumor heterogeneity (38-40), different naïve (DMSO treated) GBM lines display distinct MIEL profiles making it hard to compare drug induced profile changes (Supplementary Fig. 6d). Through linear normalization of the feature space to the profile of DMSO treated cell the naïve states are equalized and drug induced changes are visualized using a polar plot. In this plot, treatments for each cell line are represented as vectors with a magnitude - rho (the distance from the center) and directionality given by the angular coordinate theta. Applying this normalization showed that individual drugs induce similar profile alterations across different GBM lines (Supplementary Fig. 6e). This was

further demonstrated through discriminant analysis which distinguished drugs with distinct functions such as EZH1/2i and SIRTi (5 and 3 compounds respectively, 3 replicates per compound, 4 GBM lines; Fig. 2E). However, we were unable to separate subclasses of drugs with similar functions such as class I and pan HDACs inhibitors (6 and 17 compounds, 3 replicates each, 4 GBM lines) across multiple lines (Fig. 2e). These results demonstrate the ability of MIEL to correctly categorize by function drugs with varying degrees of potency across multiple cells lines.

MIEL helps identify the mechanism of drug function

Our analysis indicated that the magnitude of drug induce profile changes, as measured by distance from DMSO replicates, varies between individual drugs within each drug class (Supplementary Fig. 7a). To test whether these differences are biologically meaningful we correlated MIEL based activity with a measurable functionality. Eepigenetic drugs are often designed to work as part of a drug combination treatment. (Dong Hoon Lee, Oncotarget, 2017, additional refs). One common approach, is to use epigenetic drugs to sensitive tumor cells to standard of care cytotoxic treatments (41-44), for glioblastoma these are radiation and Temozolomide (TMZ). To identify drug classes which sensitize GBM TPCs to cytotoxic therapy, GBM2 cells were treated with epigenetic drugs for 2 days prior to radiation or TMZ. Cytotoxic treatment was carried for 4 days at levels inducing 50% reduction in cell numbers (1Gy or 200uM TMZ; Fig. 3a). At the end of the days 6 treatment, cells were score and combined drug index (CDI) was calculated (see Methods). Though we did not identify any drugs which synergized (CDI<0.7) with the radiation therapy (Fig. 3b, right panel) multiple drugs from both PARPi and BETi categories that sensitized the cells to TMZ treatment (Fig. 3b, left panel).

PARP inhibitors have been extensively studied in this context and were shown to function through multiple non epigenetic mechanisms such as PARP trapping (45-47). Consistent with this, most PARPi did not induce epigenetic changes detectable using MIEL (Fig. 3d, Supplementary Fig. 7b) and we found no correlation between the magnitude of epigenetic changes as measured by MIEL and CDI (Fig. 3d). To date only a single report utilizing the BETi OTX015 (48) has pointed to a synergistic effect with TMZ, prompting us to validated this finding in additional GBM lines. In all we tested 6 GBM lines, in 3 of these (454M, PBT24 and GBM2) the BET inhibitors increased the effectiveness of the TMZ treatment (Fig. 3c). In the other 3 lines (SK262, 101A and 217M) these drugs did not induce synergism, and in many cases were found to be protective against (CDI>1), the TMZ treatment (Fig. 3c). Though only few BETi induced epigenetic changes during our initial screen conducted over 24 hours, we found that a 6 days treatment led to significant epigenetic changes in all cell line tested (Fig. 3d, Supplementary Fig. 7b). In lines displaying synergism between TMZ and BETi, we found a significant correlation between the degree of BETi activity as measure by MIEL and the degree of synergism (Fig. 3d). This demonstrates that the ranking achieved by MIEL for individual compounds can predict relative drug activity and suggests an epigenetic component for the mechanism of BETi-TMZ synergy.

The enzyme O^6-alkylguanine DNA alkyltransferase (MGMT), which provides the main line of defense against DNA alkylating agents such as TMZ, has been found to be epigenetically silenced through DNA methylation in a large fraction of GBM tumors (49, 50). To gain a better understanding of the mechanism of by which BETi sensitize GBM TPCs to TMZ treatment we quantified the expression of MGMT in the 6 lines tested using qPCR. This analysis showed that while all 6 lines express similar levels of BET TFs such as Brd2 (Fig. 3e) and are thus susceptible to BET inhibitors, only the 3 lines displaying BETi-TMZ synergism express MGMT (Fig.3e). We found that treating those with BETi dramatically reduced the expression of MGMT in the synergistic lines (Fig. 3f). Finally, combining BET inhibitors with the MGMT inhibitor Lomeguatrib did not increase sensitivity to TMZ above the levels conferred by Lomeguatrib alone (Fig. 3g).

Taken together these results suggest that BETi can increase the effectiveness of TMZ treatment by reducing the expression of MGMT and demonstrate the power of MIEL to provide critical information on the mechanism of drug function (i.e. epigenetic mechanism of BETi but not PARPi).

Discussion

Here we show that phenotypic profiling of chromatin organization and histone modification patterns visualized by immunofluorescence for specific histone modifications enables detection and functionality based categorization of active epigenetic drugs. High content assays are not commonly used for screening epigenetic compounds and often employ reporter-based studies in which compounds are chosen on their ability to alter the expression of a silenced reporter (34). In cases where immunofluorescence for specific histone modifications was employed, the assays focused on changes in average intensity-based analysis (35). We demonstrated that machine learning approach based on image texture (i.e. MIEL) dramatically improves the accuracy of active compounds detection compared to the intensity based thresholding and has a significant advantage for functional categorization and prediction. MIEL does not involve any additional steps during assay preparation, and therefore no additional costs, thus representing a clear advantage of intensity thresholding.

Curiously, a number of compounds from several functional categories did not induce detectable epigenetic changes, which could have several potential explanations. This can represent a bias emanating from the cellular system chosen and its distinctive expression profile. For example, it was previously shown that, GBM TPCs, maintain high Class I HDACs expression and down regulate Class II HDACs expression (51). Alternatively, this may represent differences between the kinetics of drugs from different functional classes or the turn-over rate of specific histone modifications (52). For example, our initial screen was conducted over 24 hours, and detected epigenetic changes only for the few BET inhibitors also inducing high toxicity. However, when tested after 6 days of treatment, we found that almost all BETi induce significant epigenetic changes detectable by MIEL.

Previous studies have shown that image based profiling was able to distinguish between compound classes with very distinct function such as Aurora and HADC inhibitors (20). One objective of our study was to estimate the resolution of separation between compound categories with similar functions. We found that a single histone modification was sufficient to separate highly distinct classes. Separating similar classes, such as Aurora and JAK inhibitors affecting histone phosphorylation or Pan and Class I HADCs which affect histone acetylation, required staining for at least one additional histone modification. Despite their many advantages, cellular assay, including high content assays, are often used as secondary screens for epigenetic drugs due multiplicity of enzyme family members and inability to determine direct enzymatic activity (10). The ability to separate closely related functional categories on top of other advantages offered by the MIEL profiling approach make it an attractive alternative for primary screens.

Phenotypic profiling methods have been previously used to identify genotype□specific drug responses by comparing profiles across multiple isogenic lines (53). Here we show that activity of 57 compounds was significantly correlated across 4 different primary GBM lines, that variation in activity levels correlated with level of target expression and that the various categories can be distinguished across cell lines. Together, these suggest that MIEL can be used to identify cell lines which show an aberrant reaction to selected drugs and aid in identifying optimal treatments to individual patients. Similar applications were previously used to tailor specific kinase inhibitors to chronic lymphocytic leukemia (CLL) patients displaying venetoclax resistance (54).

Our results show a significant correlation between BET inhibitor activity, as defined by MIEL, and their ability to synergize and increase sensitivity of TPCs to TMZ, thus demonstrating the ability of MIEL to be used as a secondary screening assay for hit prioritization. This analysis also uncovered a previously unknown role for BET inhibitors in reducing the expression of MGMT. Previous studies have demonstrated upregulation of several BET transcription factors in glioblastomas (55, 56) and multiple pre-clinical studies have investigate the potential of BET inhibition as a single drug treatment for GBM (57-59). However, while clinical trials with the BET inhibitor, OTX015, demonstrated low toxicity at doses achieving biologically active levels, no detectable clinical benefits were found (60). This prompted multiple drug combination approaches (61) such as a combined HDACi and BETi treatment (62, 63). The mechanism by which BETi can induce increased TMZ has not been described. Recently, a distal enhancer regulating MGMT expression was identified (64). Activation of this enhancer by targeting a Cas9-p300 fusion to its genomic locus increases MGMT expression while deletion of this enhancer reduced MGMT expression (64). BET transcription factors bind the elevated levels of H3K27ac found in enhancers (65, 66), suggesting a possible mechanism for BETi induced reduction of MGMT expression which in turn results in increased sensitivity to the DNA alkylating agent TMZ. Silencing of the MGMT gene through promoter methylation has long been known to increase responsiveness to TMZ treatment and improve prognosis in GBM patients (24, 49, 50). Despite that,

clinical trials combining TMZ and MGMT inhibitors did not produce improved therapeutic outcomes in glioblastoma patients, possibly due to the 50% reduction in TMZ dose required to avoid hematologic toxicity with that combination (67-69). Further pre- and clinical trial are needed to determine whether the elevated sensitivity of glioblastoma to BETi and their ability to reduce MGMT expression can be exploited to improve the clinical outcome of GBM patients.

High content profiling methods have become eminent tools for drug discovery. At the same time, epigenetic writers, erasers and reader are the focus of multiple campaigns and numerous pre and clinical trials testing the benefits of such drugs are being conducted. We believe that MIEL as a method for profiling the endogenous patterns of histone modifications and chromatin organization can greatly improve drug discovery efforts in this field.

Materials and Methods

Cell Culture: Monolayer cultures of patient-derived GMB TPCs were propagated on Matrigel-coated plates in DMEM:F12 Neurobasal media (1:1; Gibco), 1% B27 supplement (Gibco), 10% BIT 9500 (StemCell Technologies), 1 mM glutamine, 20 ng/ml EGF (Chemicon), 20 ng/ml bFGF, 5 µg/ml insulin (Sigma), and 5 mM nicotinamide (Sigma). The medium was replaced every other day and the cells were enzymatically dissociated using Accutase prior to splitting.

Immunofluorescence: Cells were rinsed with PBS and fixed in 4% paraformaldehyde in PBS for 10 min at room temperature. After blocking with PBSAT (2% BSA and 0.5% Triton X-100 in PBS) for 1 h at room temperature, the cells were incubated overnight at 4°C with primary antibodies diluted in PBSAT. The primary antibodies are listed in Table 1, and the appropriate fluorochrome-conjugated secondary antibodies were used at 1:500 dilution. Nuclear co-staining was performed by incubating cells with DAPI nuclear dye.

Microscopy and image analysis: For MIEL analysis cells were imaged on an IC200-KIC (Vala Sciences) using a ×20 objective. Images collected were analyzed using Acapella 2.6 (PerkinElmer). At least 5 fields per well were acquired and at least 2 wells per population were used. Features of nuclear morphology, fluorescence intensity inter-channel co-localization, and texture features (Image moments, Haralick, Threshold Adjacency Statistics) were calculated using custom algorithms (scripts available

from www.andrewslab.ca). A full list of the features used is available from the authors. Values for each cell were generated and exported to Microsoft Excel for further analysis.

Data processing: The image features based profile for each cell population (eg, cell types, treatments, technical repetition, etc.) was represented using a vector (center of distribution vectors) in which every element is the average value of all cells in that population for a particular feature. The vector's length is given by the number of features chosen (262 per histone modification). Raw feature values were normalized by z-scoring to the average and standard deviation of all populations being compared. All cells in each population were used to calculate center vectors and each population contained at least 50 cells. Activity level for each drug was determined by calculating distance from DMSO. For this, feature values of all DMSO replicates center vectors were used to calculate the 'DMSO center vector'. Euclidean distance of each compound and each DMSO replicate to the 'DMSO center vector' was calculated. Distances were z-scored scored to the average distance and standard deviation of DMSO replicates from the 'DMSO center vector'. Transcriptomic based profile for each cell population was represented using a vector in which every element is the z-scored FPKM value for a single gene in that population. The length of the vector is given by the number of genes used to construct the profile.

MDS: The Euclidean distance between all vectors (either image features or transcriptomic based) was calculated to assemble a dissimilarity matrix (size N×N, where N is the number of populations being compared). For representation, the N×N matrix was reduced to a Nx2 matrix with MDS using the Excel add-on program xlstat (Base, v19.06), and displayed as a 2D scatter plot.

Epigenetic Drugs Screen: GBM2 cells were plated at 4000 cells/well and exposed to Epigenetics compounds (Table 2) at 10 µM for 1 days in 384-well optical bottom assay plates (PerkinElmer). Negative controls were DMSO (0.1%), 48 DMSO replicates per plate, 3 technical replicates (wells) were treated per compound. Cells were fixed and stained with histone modification specific antibodies (H3K27ac & H3K27me3, H3K9me3 & H3K4me1; Table 1) and AlexaFluor-488- or AlexaFluor-555-conjugated secondary antibodies. DNA was stained with DAPI followed by imaging and feature extraction. To compare data from multiple plates, average feature values in each plate were was normalized DMSO. For this, feature values of all DMSO replicates center vectors in each plate were used to calculate the 'plate-wise DMSO vector'. Raw feature values for all center vectors of all populations in each plate were normalized to the plate-wise DMSO vector; normalized feature values were z-scored as above. To identify active compounds, activity level for each compounds was calculated as above and active compounds were defined as compounds for which activity z-score was >3. Compounds reducing the number of imaged cell per well below 50 were considered toxic and excluded from analysis.

Concentration Curve: For concentration curves GBM2 cells were plated and stained as above. For each compound (Table 3), cells were treated at 0.1, 0.3, 1.0, 3.0, 10.0 uM. Activity levels were calculated as above. For comparing epigenetic changes and toxicity, average cell count over all replicates for each compound was calculated. Cell counts were z-scored against the average and the standard deviation of all DMSO replicates. Distances (z-scored) and cell counts (z-scored) were averaged for each functional class at each concentration.

RNAseq and transcriptomic analysis: Total RNA was isolated from GBM2 cells using the RNeasy Kit (Qiagen), 0.25 ug total RNA was used for isolation of mRNAs and library preparation. Library preparation and sequencing was conducted by the SBP genomics core (Sanford-Burnham NCI Cancer Center Support Grant P30 CA030199). PolyA RNA was isolated using the NEBNext® Poly(A) mRNA Magnetic Isolation Module and barcoded libraries were made using the NEBNext® Ultra II™ Directional RNA Library Prep Kit for Illumina®(NEB, Ipswich MA). Libraries were pooled and single end sequenced (1X75) on the Illumina NextSeq 500 using the High output V2 kit (Illumina). Read data was processed in BaseSpace (basespace.illumina.com). Reads were aligned to Homo sapiens genome (hg19) using STAR aligner (https://code.google.com/p/rna-star/) with default settings. Differential transcript expression was determined using the Cufflinks Cuffdiff package (https://github.com/cole-trapnell-lab/cufflinks). For heat maps showing fold change in expression the FPKM values in each drug treated population were divided by the average FPKM values of DMSO treated GBM2 and values are shown as log2 of the ratio. Heat maps were generated using Microsoft Excel conditional formatting function.

Discriminant Analysis: Quadratic discriminant analysis was conducted using the Excel add-on program xlstat (Base, v19.06). Model was generated in a stepwise (forward) approach using default parameters. All features derived from images of tested histone modification were used for analysis following normalization by z-score. Features displaying multicollinearity were reduced. Model testing was done by cross validation by ‘leave one out’ method.

Polar plots: Due to the inherent heterogeneity of TPC lines, we performed data normalization when comparing multiple treatments on several TPC lines. For this, the value of each feature for all individual cells in each line was divided by the average value obtained for that feature in the DMSO treated population from the same cell line. Therefore, following normalization, untreated cells from all lines had the same center of distribution vector (in which all elements are equal to 1), while each treatment retained its relative distance from untreated as well as from all other treatments of the same cell line. However, as each cell line is divided by a different value, the distance vectors originating from two different lines represent the change in feature values induced by treatment, rather than the absolute feature values. Therefore, following MDS, the results are shown on a polar plot to indicate that the various treatments induce similar feature value changes in multiple lines rather than similar absolute

values. As a result, direction and distance to the origin are comparable between lines while distances directly between points are not.

Comparing epigenetic changes in different cell lines: For comparing drug induced epigenetic changes across multiple GBM lines 101A, 217M, GBM2 and PBT24 cells were plates at 4000 cells/well and treated with compounds for 24 hours. Compounds and concentrations are shown in Table 4. Feature values for each cell lines were normalized to average DMSO feature values of that line prior to data processing. Activity level was calculated as above. Pearson coefficient and significance of correlation for activity levels in each pair of cell lines were calculated using the Excel add-on program xlstat (Base, v19.06).

Correlation of transcriptomic and image-based profiles: Euclidean distance between DMSO, VA (15uM), SAHA (3uM) and TSA (1uM) treated GBM2 cells (triplicates for each) was calculated using either transcriptomic data (FPKM) or texture features. Pearson's correlation coefficient (R) was transformed to a t-value using the formula (t = R × SQRT(N-2)/SQRT(1-R2) where N is the number of samples, and R is Pearson correlation coefficient, and the p-value was calculated using Excel t.dist.2t(t) function.

Sensitization to radiation or TMZ : Cells were plated at 1500 cells/well in 384-well optical bottom assay plates (PerkinElmer). 2 sets of the experiment were prepared; negative controls were DMSO (0.1%), 48 DMSO replicates per plate; 3 replicates (wells) were treated per compound. Compound concentrations used are shown in Table 5. Cells in both sets were pre-treated with epigenetic compounds for 2 days prior to cytotoxic treatment. Cytotoxic treatment, either 200uM Temozolomide (TMZ, Sigma) or 1Gy x-ray radiation (RS2000; RAD Source) was carried out for 4 days on single set ('treatment set'); for TMZ treatment DMSO was given to the second set ('control set'). Radiation was given as a single dose at day 3; TMZ was given twice at the 3rd and 5th day of the experiment. Cells were fixed, stained with DAPI and scored automatically using an automated microscope (Celigo; Nexcelom Bioscience). For each compound the fold change in cell number was calculated for both the 'treatment set' (Drug+Cytotox) and the 'control set' (Drug) compared to DMSO treated wells in the 'control set'. The effect of Radiation or TMZ alone was calculated as fold reduction of DMSO treated wells in the 'treatment set' compared to DMSO treated wells in the 'control set'(Cytotox). Coefficient of drug interaction (CDI) was calculated as: (Drug+Cytotox)/ (Drug)X(Cytotox). For conformation experiments, same regiment and CDI calculations were carried out on SK262, 101A, 217M, 454M and PBT24 GBM lines; PARPi and BETi were used at same concentration as initial screen on GBM2 (Table 5).

Acknowledgments

We are thankful to Harley Kornblum (UCLA) for sharing multiple primary human GBM lines, to Alysson Muotri (UCSD) for providing fibroblast, iPSC and NPC lines, and Bradley Bernstein (MGH Harvard) for sharing MGGTPCs and MGG-DGCs lines. We owe a debt of gratitude to Susanne Heynen-Genel and other members of the High-Content Facility at CPCCG for their invaluable help with cell imaging and to Brian James and Kang Liu at the SBP Genomics core for their help with library preparation and RNA sequencing (NCI Cancer Center Support Grant P30 CA030199). This work was supported by sponsored research agreement with Celgene and an R01 NS066278 to A.V.T and by a CIHR Foundation grant FDN143312 and a Tier 1 Canada Research Chair in Membrane Biogenesis award to D.W.A.

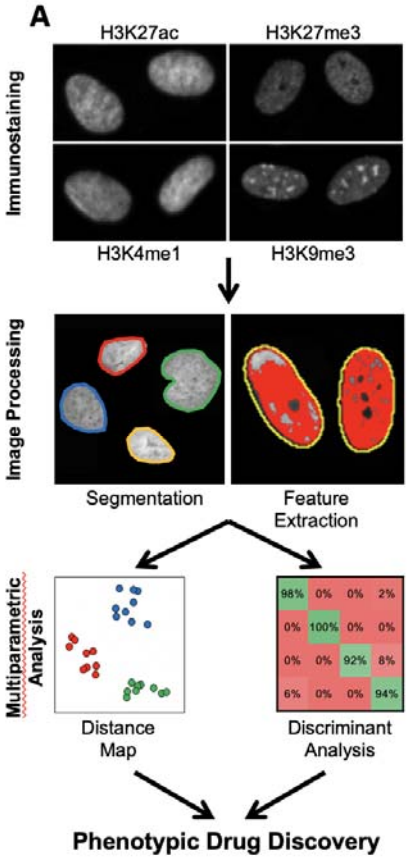

B

	#	Toxic	Detection (%) MIEL	Intensity
DMSO	91	0	0	0
L3MBTL	3	0	0	0
PIM	4	2	0	0
PRMT	5	0	0	0
KMT-DotL1	3	0	0	0
BRPF	3	0	0	0
MLL	5	0	20	0
KDM-Misc	4	0	25	0
KDM-JMJC/D	8	0	25	0
PARP	10	0	20	10
HAT	10	0	30	0
BET	12	0	42	25
KMT-Misc	7	3	25	0
DNMT	10	1	44	22
KDM-LSD1	4	0	50	0
SIRTi	12	0	58	50
KMT-G9a/GLP	9	3	67	33
KMT-EZH1/2	10	0	90	70
JAK	19	4	87	60
SIRTa	7	1	83	83
HDAC6	3	0	100	67
Aurora	19	5	100	93
HDAC-Pan	47	0	85	81
HDAC-Class I	7	1	100	100

H3K27me3 / H3K27ac / H3K9me3 / H3K4me1

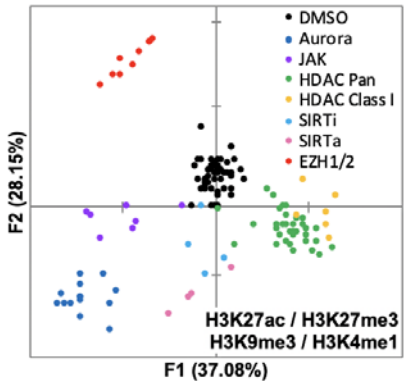

D

	#	DMSO	Aurora	JAK	HDAC Pan	HDAC Class I	SIRTa	SIRTi	EZH1/2
DMSO	48	100	0	0	0	0	0	0	0
Aurora	14	0	86	0	0	0	7	7	0
JAK	8	0	0	88	0	0	13	0	0
HDAC Pan	40	5	0	0	90	3	0	3	0
HDAC Class I	5	0	0	0	0	100	0	0	0
SIRTa	4	0	0	0	0	0	75	25	0
SIRTi	4	25	0	0	0	0	25	50	0
EZH1/2	9	0	0	0	0	0	0	0	100
Total	132								

H3K27ac / H3K27me3
H3K9me3 / H3K4me1

E

	DMSO	Phospho	HDAC	SIRT	EZH2	DMSO	Phospho	HDAC	SIRT	EZH2
	H3K9me3					H3K4me1				
DMSO	100	0	0	0	0	98	0	0	0	2
Phospho	5	73	0	9	14	18	68	0	9	5
HDAC	7	4	87	2	0	9	7	78	7	0
SIRT	13	0	0	88	0	13	13	0	75	0
EZH2	56	22	0	0	22	67	11	0	0	22
	H3K27me3					H3K27ac				
DMSO	96	4	0	0	0	100	0	0	0	0
Phospho	36	55	0	9	0	0	91	0	5	5
HDAC	13	2	80	2	2	2	0	89	4	4
SIRT	13	0	0	88	0	13	0	0	88	0
EZH2	0	0	11	0	89	33	0	0	0	67

Figure 1.

Fig. 1: MIEL compares the epigenetic landscape of multiple cell populations and can be used to detect active epigenetic drugs across cell lines and drug concentrations.

(a) Flowchart of MIEL pipeline. Fixed cells were immunostained for the desired epigenetic modifications, stained with Hoechst 33342 to visualize DNA and imaged. Nuclei were segmented based on DNA staining, and texture features calculated from the pattern of immunofluorescence. The relative similarity of multiple cell populations was assessed by calculating the multiparametric Euclidean distance between their pairwise centers, and represented in 2D following MDS (distance map). Discriminant analysis is trained on features derived from the histone staining texture of drug treated cells and categorized by drug function. (b) Table showing the fraction of epigenetic drugs in each functional category identified as active by either MIEL analysis employing texture features derived from images of GBM2 cells stained for H3K9me3, H3K4me1, H3K27ac, H3K27me3 or by intensity based analysis using the same modifications (see Methods). (c,d,e) Quadratic discriminant analysis using texture features derived from images of GBM2 cells treated with either DMSO or 84 active compounds (n=132 total cell populations, 84 compounds represented as the average of 3 replicates, 48 DMSO replicates) stained for H3K9me3, H3K27me3, H3K4me1, H3K27ac. (c) Scatter plots depict the first 2 discriminant factors derived from features of all four histone modification images for each cell population (drug). (d) Confusion matrix showing results of cross validation by ‘leave one out’ method for analysis in ‘c’, numbers depict the percent of drugs in each category. (e) Confusion matrix showing results of cross validation for a discriminant analyses conducted using features from a single histone modification.

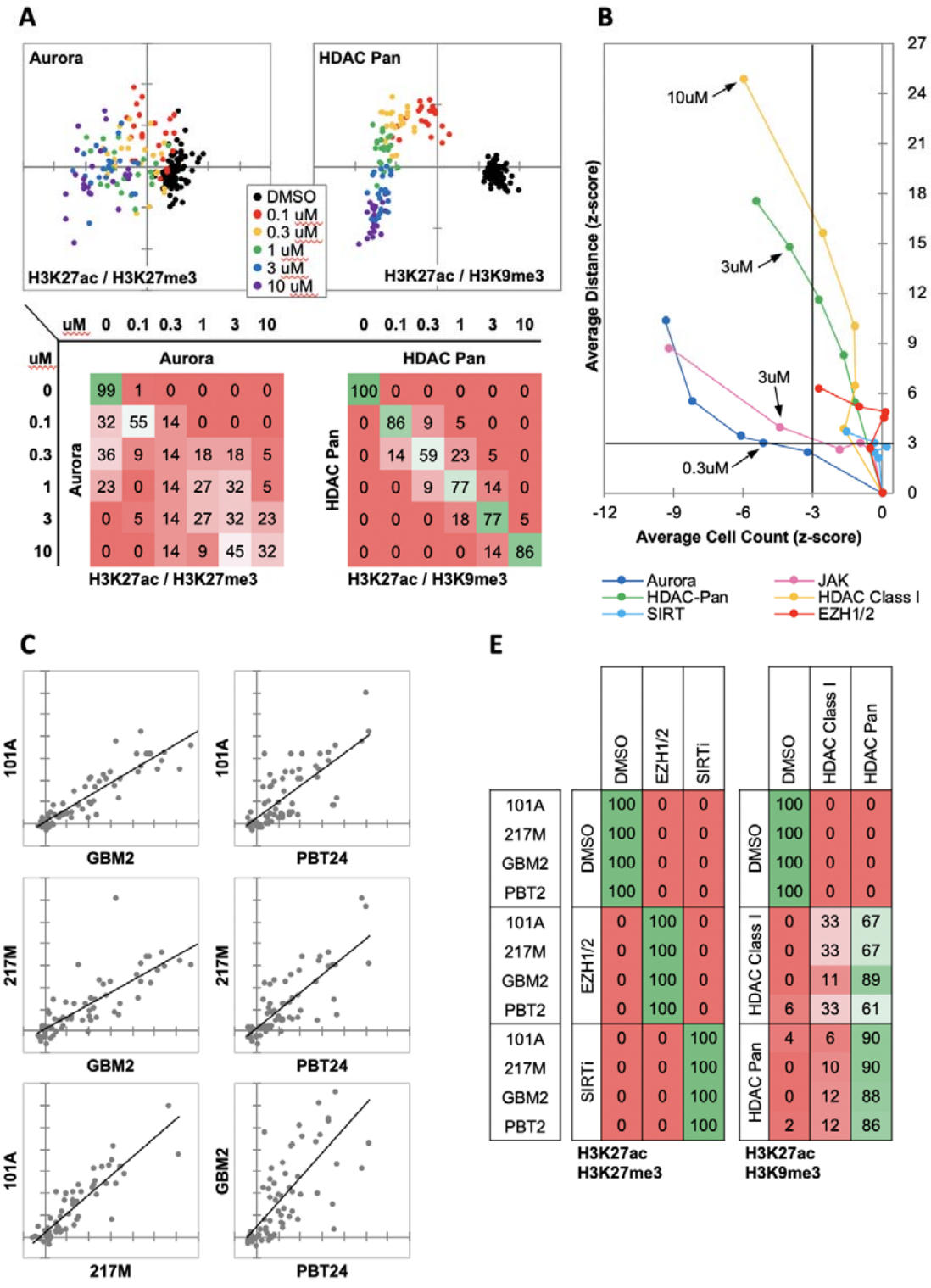

Figure 2.

Fig. 2: MIEL distinguishes between multiple categories of epigenetic drugs.

(a) Quadratic discriminant analysis using texture features derived from images of GBM2 cells treated with 0.1, 0.3, 1, 3 or 10uM Aurora (n=11 compounds, 2 replicates) or HDAC Pan inhibitors (n=11 compounds, 2 replicates) stained for H3K9me3, H3K27me3, H3K4me1, H3K27ac. Scatter plot depict the first 2 discriminant factors for each cell population (drug replicate). Confusion matrix showing results of cross validation of by 'leave one out' method (numbers depict the percent of replicates). (b) Scatter plot comparing the magnitude of effect, as calculated using average z-scored Euclidean distances from DMSO, to drug induced cytotoxicity, as calculated using z-scored average cell count. Euclidean distance was calculated using image texture features derived from images of H3K27ac & H3K27me3 (Aurora) or H3K27ac & H3K9me3 (HDAC Pan). Distances and cell counts represent average of all compounds in each category; n_{Aurora}=11, $n_{EZH1/2}$=5, $n_{HDAC\ Class\ I}$=7, $n_{HDAC\ Pan}$=43, n_{JAK}=15, n_{SIRTi}=4). (c) Scatter plots comparing the average z-scored Euclidean distances from DMSO replicates across four GBM lines (n=57 compounds, z-score for each compound is the average of 3 technical replicates). Euclidean distances were calculated using image texture features derived from images of H3K27ac & H3K27me3 or H3K27ac & H3K9me3. (d) A table summarizing the Pearson coefficient and statistical significance of z-scored Euclidean distances shown in 'c'. (e) Confusion matrixes showing results of cross validation by 'leave one out' method (numbers depict the percent of replicates) for a quadratic discriminant analysis using texture features derived from images of GBM2, PBT24, 101A, 217M cells. Left: Cells were treated with either DMSO, 5 EZH1/2 inhibitors or 2 SIRT inhibitors (n=33 total cell populations for each cell line, 12 DMSO replicates, 3 replicates for per compound) features derived from images of cells stained for H3K27me3, H3K27ac. Right: Cells treated with either DMSO, 6 Class I HDAC inhibitors or 17 Pan HDAC inhibitors (n=70 total cell populations for each cell line, 12 DMSO replicates, 3 replicates for per compound) features derived from images of cells stained for H3K27ac, H3K9me3.

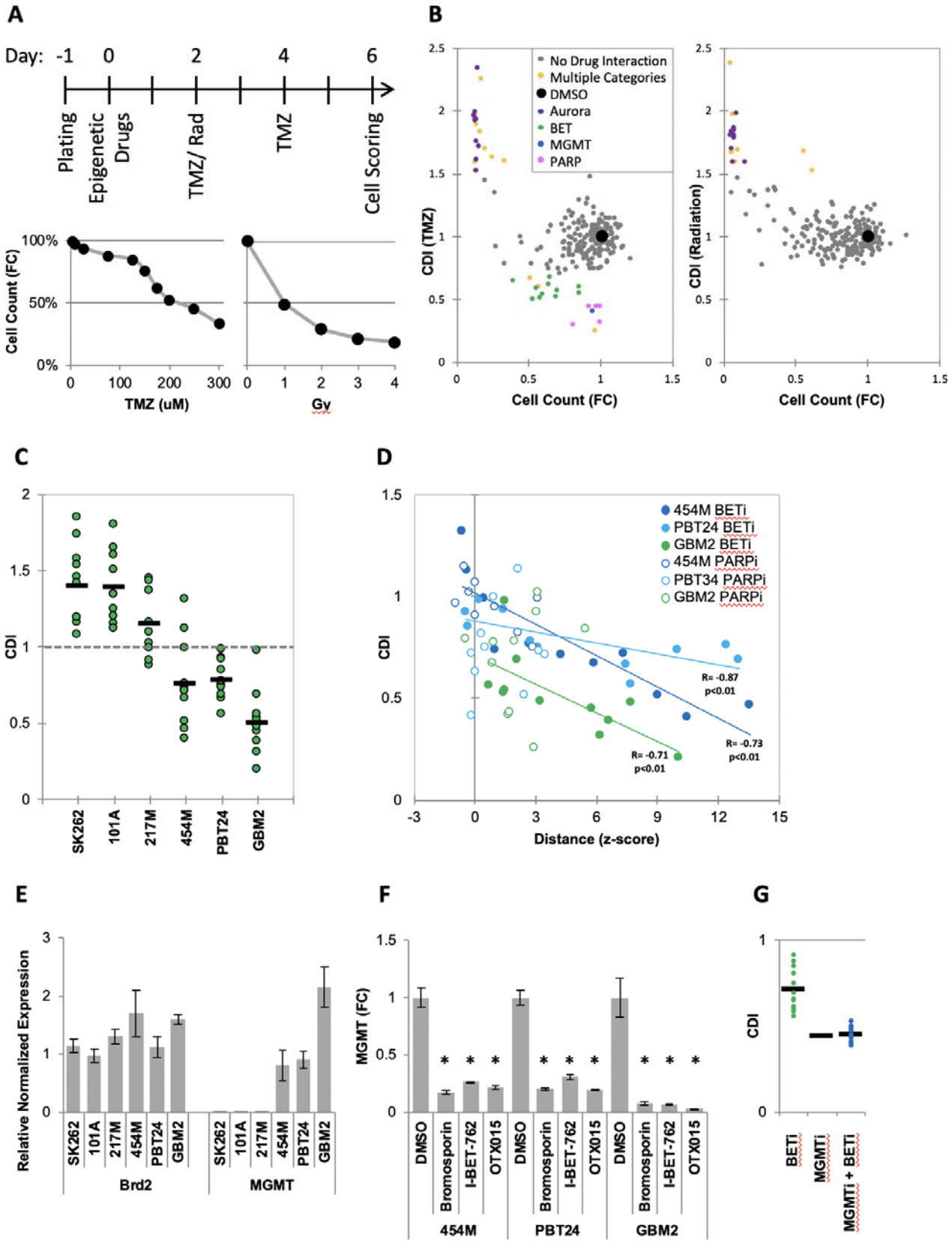

Figure 3.

Fig. 3: MIEL can be used to rank candidate drugs by activity

(a) Top: Scheme describing the experimental setup used to identify synergy between epigenetic drugs and radiation or TMZ. Bottom: Scatter plots showing the fold reduction in GBM2 cell count following a 4 days treatment with varying concentration of TMZ and radiation doses. (b) Scatter plots showing fold change in cell count (compared to DMSO treated cells) and coefficient of drug interaction (CDI) for synergy with TMZ (left) and radiation (right) for each drug (n=222, values represent the average of 3 technical replicates). (c) Graph showing individual and average CDI for BET inhibitors in 6 GBM lines (n=11 drugs, values represent the average of 3 technical replicates). (d) Scatter plot showing the correlation between CDI and MIEL derived activity (z-scored Euclidean distance from DMSO) of BET and PARP inhibitors (n_{BETi}=11; n_{PARPi}=10; values represent the average of 3 technical replicates) in 3 GBM lines. (e) Bar graph showing the relative normalized expression of Brd2 and MGMT in 6 GBM lines (Mean±SD; n=3 technical repeats). (f) Bar graph showing fold reduction in MGMT expression following treatment with BET inhibitors in 3 different GBM lines (Mean±SD; n=3 technical repeats). (g) Graph showing individual and average TMZ sensitization CDI for BETi, MGMTi (Lomeguatrib) and BETi & MGMTi in GBM2 cells (n=11 drugs, values represent the average of 3 technical replicates).

A

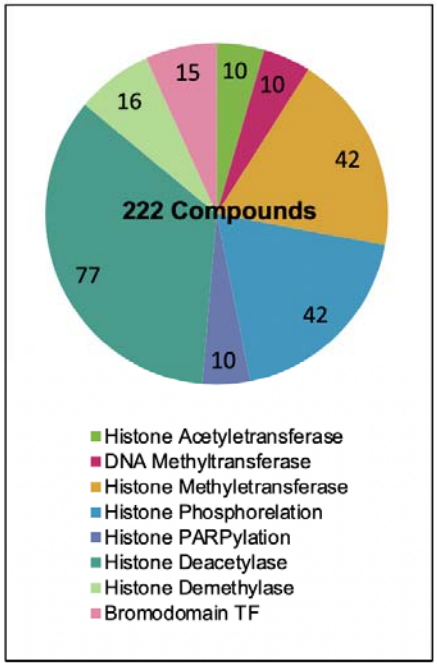

B

Category	Target Class	#
Histone Acetyletransferase	HAT	10
DNA Methyltransferase	DNMT	10
Histone Methyletransferase	DotL1	3
	EZH1/2	10
	G9a/GLP	9
	SetD	3
	L3MBTL	3
	PRMT	5
	MLL	5
	Other	4
Histone Phosphorelation	Aurora	19
	JAK	19
	PIM	4
Histone PARPylation	PARP	10
Histone Deacetylase	HDAC-Class I	15
	HDAC6/8	4
	Pan	39
	SIRTi	12
	SIRTa	7
Histone Demethylase	JMJC/D	8
	LSD1	4
	Other	4
Bromodomain	BET	12
	BRPF	3

Supplementary Figure 1.

Supplementary Fig. 1

(a) Pi chart showing functional classes of epigenetic drugs used in the study. (b) Table detailing the molecular targets of epigenetic drugs used in the study.

A

	#	Toxic	MIEL H3K27me3	MIEL H3K27ac	MIEL H3K9me3	MIEL H3K4me1	Intensity H3K27me3	Intensity H3K27ac	Intensity H3K9me3	Intensity H3K4me1
DMSO	91	0	0	0	0	0	0	0	0	0
L3MBTL	3	0	0	0	0	0	0	0	0	0
PIM	4	2	0	0	0	0	0	0	0	0
PRMT	5	0	0	0	0	0	0	0	0	0
KMT-DotL1	3	0	0	0	0	0	0	0	0	0
BRPF	3	0	0	0	0	0	0	0	0	0
MLL	5	0	0	0	20	0	0	0	0	0
KDM-Misc	4	0	0	0	25	0	0	0	0	0
KDM-JMJC/D	8	0	0	0	25	0	0	0	0	0
PARP	10	0	0	10	10	10	0	0	10	0
HAT	10	0	0	20	0	10	0	0	0	0
BET	12	0	0	17	25	17	0	0	25	8
KMT-Misc	7	3	0	25	25	25	0	0	0	0
DNMT	10	1	22	22	44	22	11	0	22	11
KDM-LSD1	4	0	25	25	50	25	0	0	0	0
SIRTi	12	0	33	25	50	42	8	0	42	50
KMT-G9a/GLP	9	3	33	50	50	33	0	0	33	0
KMT-EZH1/2	10	0	90	60	60	60	40	0	30	0
JAK	19	4	53	73	73	73	20	7	60	40
SIRTa	7	1	67	67	67	83	50	17	67	83
HDAC6	3	0	33	100	67	100	0	67	33	67
Aurora	19	5	36	86	93	100	14	0	93	21
HDAC-Pan	47	0	74	83	83	81	66	81	51	77
HDAC-Class I	7	1	83	100	100	100	50	100	100	100

Percent Detected

B

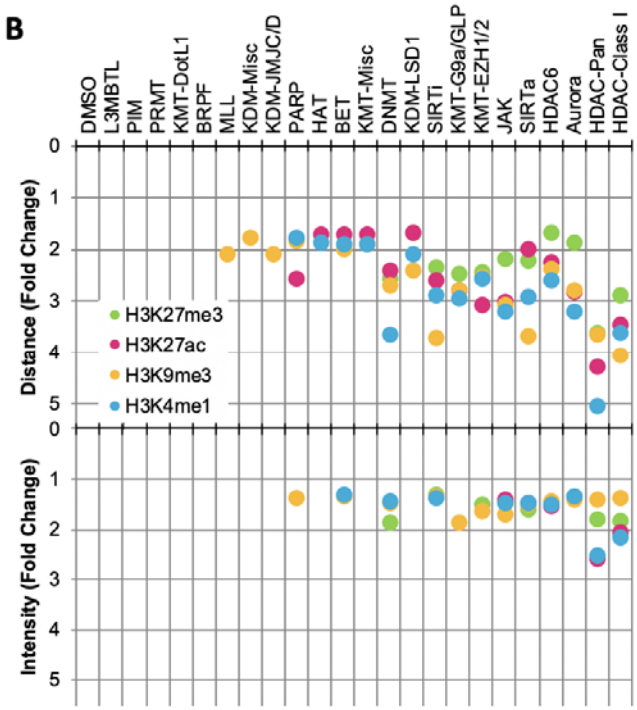

Supplementary Figure 2.

Supplementary Fig. 2

(a) Table showing the fraction of epigenetic drugs in each functional category identified as active by either MIEL analysis employing texture features derived from images of GBM2 cells stained for either H3K9me3, H3K4me1, H3K27ac, H3K27me3 or by intensity based analysis using the individual modifications (see Methods). (b) Graph depicting the average fold change in Euclidean distance from DMSO replicates induced by drugs of each functional category as calculated using texture features derived from images of individual histone modification (n for each category is shown in 'a').

A

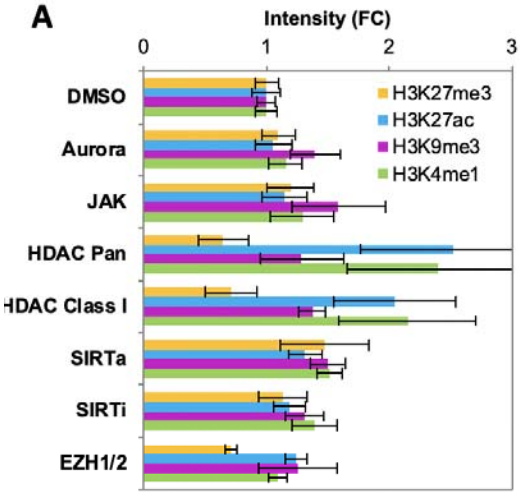

B

	#	DMSO	Aurora	JAK	HDAC Pan	HDAC Class I	SIRTa	SIRTi	EZH1/2
DMSO	48	100	0	0	0	0	0	0	0
Aurora	14	64	7	14	0	0	7	7	0
JAK	8	25	38	13	0	0	25	0	0
HDAC Pan	40	20	0	3	73	3	3	0	0
HDAC Class I	5	20	0	0	40	40	0	0	0
SIRTa	4	25	0	0	0	0	50	25	0
SIRTi	4	50	25	25	0	0	0	0	0
EZH1/2	9	22	0	0	0	0	0	0	78
Total	132								

H3K27ac / H3K27me3
H3K9me3 / H3K4me1

C

H3K9me3

	DMSO	Aurora	JAK	HDAC Class I	HDAC Pan	SIRTa	SIRTi	EZH1/2
DMSO	100	0	0	0	0	0	0	0
Aurora	7	57	21	0	0	0	0	14
JAK	0	25	38	0	0	25	0	13
HDAC Class I	0	0	0	60	40	0	0	0
HDAC Pan	8	3	3	10	75	3	0	0
SIRTa	0	0	0	0	0	50	50	0
SIRTi	25	0	0	0	0	25	50	0
EZH1/2	56	0	22	0	0	0	0	22

H3K4me1

	DMSO	Aurora	JAK	HDAC Class I	HDAC Pan	SIRTa	SIRTi	EZH1/2
DMSO	98	0	0	0	0	0	0	2
Aurora	14	57	21	0	0	0	0	7
JAK	25	25	25	0	0	13	13	0
HDAC Class I	0	0	0	60	20	0	20	0
HDAC Pan	10	3	5	3	75	0	5	0
SIRTa	0	0	0	0	0	75	25	0
SIRTi	25	0	25	0	0	50	0	0
EZH1/2	67	11	0	0	0	0	0	22

H3K27me3

	DMSO	Aurora	JAK	HDAC Class I	HDAC Pan	SIRTa	SIRTi	EZH1/2
DMSO	96	0	4	0	0	0	0	0
Aurora	43	50	7	0	0	0	0	0
JAK	25	13	38	0	0	0	25	0
HDAC Class I	20	0	0	20	60	0	0	0
HDAC Pan	13	3	0	8	73	0	3	3
SIRTa	0	0	0	0	0	50	50	0
SIRTi	25	0	0	0	0	25	50	0
EZH1/2	0	0	0	0	11	0	0	89

H3K27ac

	DMSO	Aurora	JAK	HDAC Class I	HDAC Pan	SIRTa	SIRTi	EZH1/2
DMSO	100	0	0	0	0	0	0	0
Aurora	0	71	29	0	0	0	0	0
JAK	0	63	13	0	0	0	13	13
HDAC Class I	0	0	0	60	40	0	0	0
HDAC Pan	3	0	0	5	83	0	5	5
SIRTa	0	0	0	0	0	25	75	0
SIRTi	25	0	0	0	0	75	0	0
EZH1/2	33	0	0	0	0	0	0	67

Supplementary Figure 3.

Supplementary Fig. 3

(a) Bar graph showing average fold change in average fluorescence intensity resulting from 24 hour treatment of GBM2 cells with epigenetic drugs from seven functional categories (Mean±SD; n for each category is shown in 'b'). (b) Confusion matrixes showing results of cross validation by 'leave one out' method (numbers depict the percent of replicates) for a quadratic discriminant analysis using average fluorescence intensity derived from images of GBM2 cells treated for 24 hours with either DMSO or 84 active compounds (n=132 total cell populations, 84 compounds represented as the average of 3 replicates, 48 DMSO replicates) stained for H3K9me3, H3K27me3, H3K4me1, H3K27ac. (c) Confusion matrixes showing results of cross validation by 'leave one out' method (numbers depict the percent of replicates) for a quadratic discriminant analysis using texture features derived from images of GBM2 cells treated with either DMSO or 84 active compounds (n=132 total cell populations, 84 compounds represented as the average of 3 replicates, 48 DMSO replicates) stained for H3K9me3, H3K27me3, H3K4me1, H3K27ac.

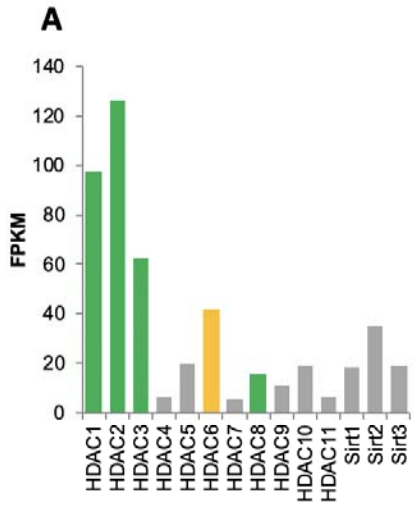

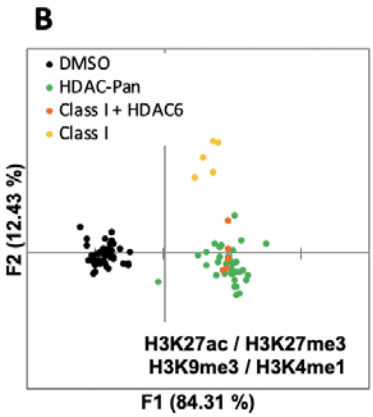

C

	#	DMSO	HDAC Pan	HDAC Class I + HDAC6	HDAC Class I
DMSO	48	100	0	0	0
HDAC Pan	35	3	91	6	0
HDAC Class I + HDAC6	5	0	80	20	0
HDAC Class I	5	0	0	0	100
Total	93				

H3K27ac / H3K27me3
H3K9me3 / H3K4me1

Supplementary Figure 4.

Supplementary Fig. 4

(a) Bar graph showing expression level (FPKM) of HDAC and SIRT genes in GBM2 cells obtained through RNA sequencing. (b,c) Quadratic discriminant analysis using texture features derived from images of GBM2 cells treated with either DMSO or 45 active compounds (n=93 total cell populations, 45 compounds represented as the average of 3 replicates, 48 DMSO replicates) stained for H3K9me3, H3K27me3, H3K4me1, H3K27ac. (b) Scatter plot depicts the first 2 discriminant factors derived from features of all histone modification images for each cell population. (c) Confusion matrix showing results of cross validation by 'leave one out' method (numbers depict the percent of compounds) for analysis in 'b'.

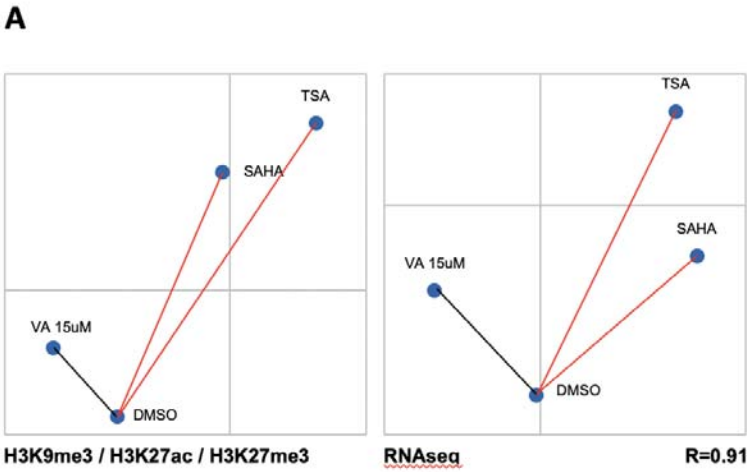

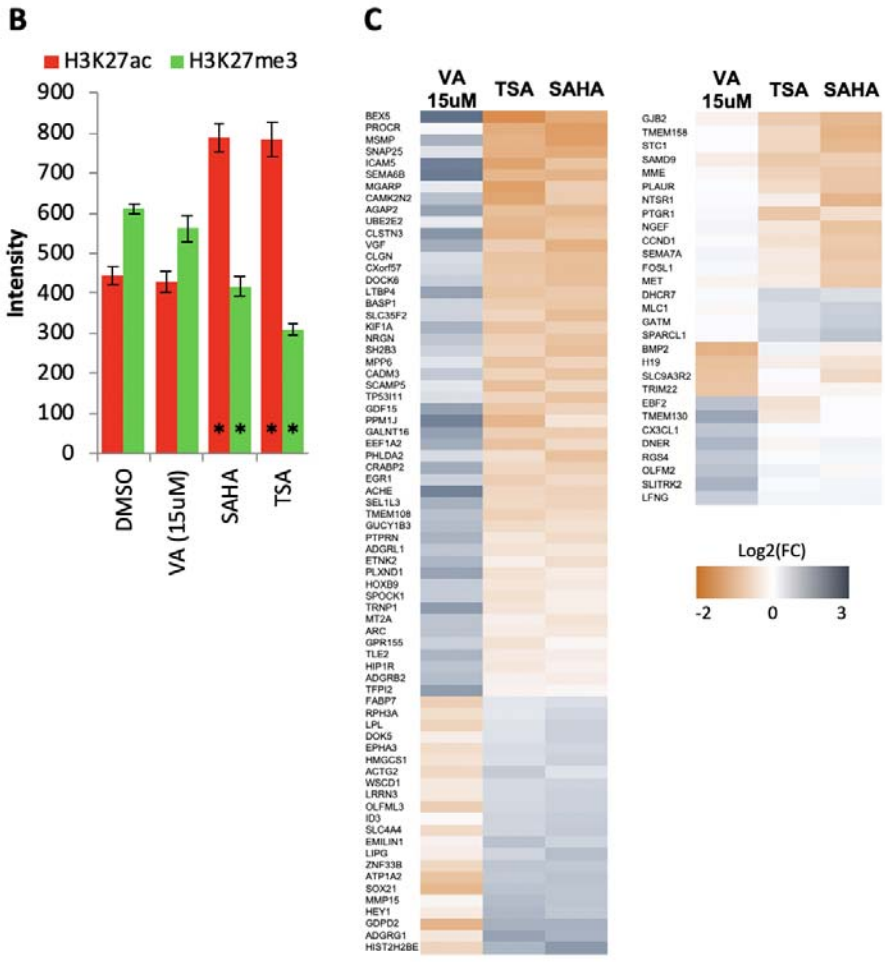

Supplementary Figure 5.

Supplementary Fig. 5

(a) Distance map depicting the relative Euclidean distances between the multiparametric centroids GBM2 cells treated for 24 hours with either DMSO, Valproic Acid (15uM), SAHA (3uM) or TSA (1uM). Left: Distances calculated using texture features derived from images of H3K9me3, H3K27ac and H3K27me3 marks. Right: Distances calculated using FPKM values of all expressed genes (13,119 genes; FPKM>1 in at least one sample). R denotes Pearson correlation coefficient. (b) Bar graph showing average fold change in average intensity resulting from 24 hour treatment of GBM2 cells with DMSO, Valproic Acid (15uM), SAHA (3uM) or TSA (1uM) (Mean±SD; n=6 technical replicates). (c) Heat maps showing log2 of fold change in expression (RNA sequencing) of select differentially expressed genes.

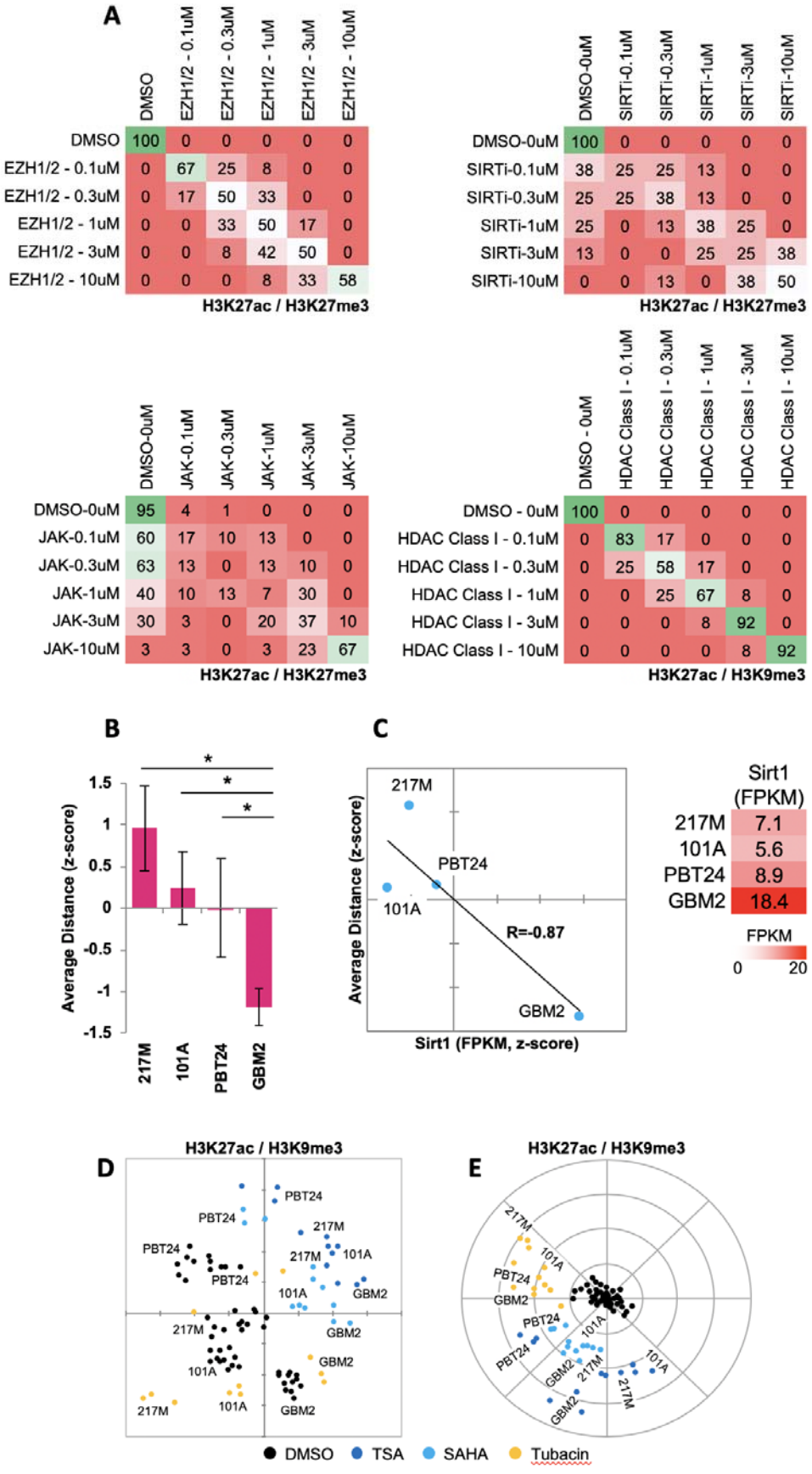

Supplementary Figure 6.

Supplementary Fig. 6

(a) Confusion matrix showing results of cross validation of by 'leave one out' method (numbers depict the percent of replicates) for a quadratic discriminant analysis using texture features derived from images of GBM2 cells treated with 0.1, 0.3, 1, 3 or 10uM of EZH1/2 (n=6), SIRT (n=4), JAK (n=15) or HDAC Class I (n=6) inhibitors (2 replicates per compound) stained for either H3K27me3 & H3K27ac (EZH1/2, JAK, SIRT) or H3K9me3 & H3K27ac (HDAC Class I). (b) Graph depicting the average z-scored Euclidean distance from DMSO replicates induced by SIRT inhibitors (n=4 compounds, 3 replicates per compound) as calculated using image texture features derived from images of 217M, 101A, PBT24 and GBM2 cells stained for H3K27ac & H3K27me3. (c) Left: Scatter plot comparing the average Euclidean distances shown in 'b' with expression of Sirt1 in each cell line (z-scored FPKM values derived by RNA sequencing). Right: table showing FPKM values for Sirt1 in the four GBM lines. (d) Distance map depicting the relative Euclidean distance between the multiparametric centroids of four GBM lines treated with either DMSO, TSA (1uM), SAHA (3uM) or Tubacin (10uM). Distances calculated using texture features derived from images of cells stained with H3K9me3 and H3K27ac (n=12 DMSO replicates; n=3 replicates per compound). (e) Polar plot visualizing the fold changes in feature values for cell populations shown in 'd' following linear normalization to DMSO averages of each cell line (see Methods).

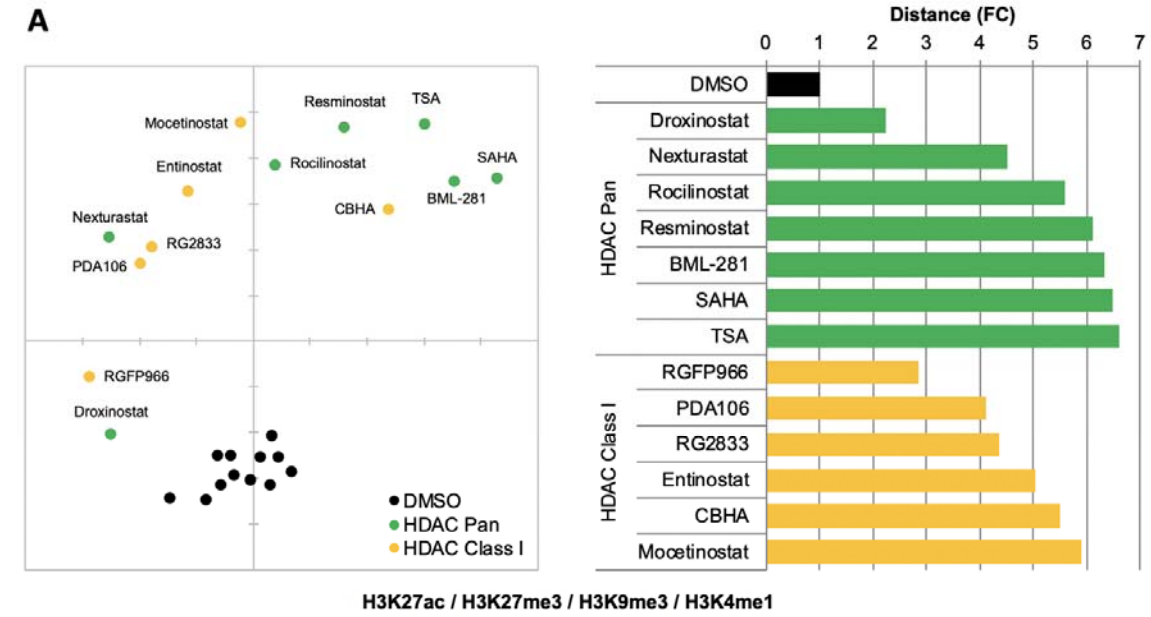

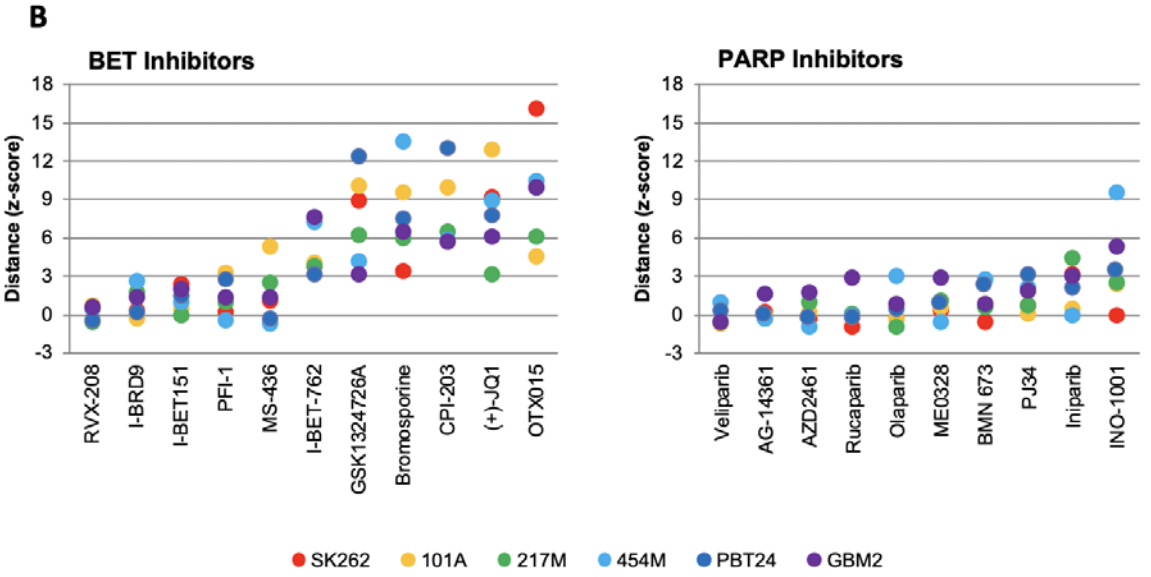

Supplementary Figure 7.

Supplementary Fig. 7

(a) Left: Distance map depicting the relative Euclidean distance between the multiparametric centroids of GBM2 cells treated with either DMSO (n=12 replicates), HDAC Pan (n=7 compounds; showing average or 3 replicates) or HDAC Class I inhibitors (n=6 compounds; showing average or 3 replicates). Distances calculated using texture features derived from images of cells stained with H3K9me3 and H3K27ac. Right: Bar graph depicting the fold change in Euclidean distance from DMSO replicates induced by drug treatments shown in ‘a’. (b) Graph depicting the average fold change in Euclidean distance from DMSO replicates induced by individual BET (left) and PARP (right) inhibitors as calculated using texture features derived from images of H3K27ac & H3K9me3 (n=3 replicates per compound).

Table 1: Primary antibodies.

Antigen	Host	Dilution	Brand	Catalogue Number
H3K9me3	rb	1:500	Active Motif	39765
H3K4me1	ms	1:250	Active Motif	39635
H3K27me3	ms	1:250	Active Motif	61017
H3K27ac	rb	1:500	Active Motif	39133
H3K27ac	ms	1:250	Active Motif	39685

Table 2: Epigenetic drug library - SBP.

Compound ID	Molecule Name	CAS Number	Functional Category
SBI-0654430	TAK-901	934541-31-8	Aurora
SBI-0654432	AMG-900	945595-80-2	Aurora
SBI-0654442	MLN8054	869363-13-3	Aurora
SBI-0654458	MK-5108 (VX-689)	1010085-13-8	Aurora
SBI-0654463	CCT137690	1095382-05-0	Aurora
SBI-0654253	Phthalazinone pyrazole	88048-62-7	Aurora
SBI-0086733	JNJ-7706621	443797-96-4	Aurora
SBI-0646927	Alisertib (MLN8237)	1028486-01-2	Aurora
SBI-0654270	ZM 447439	331771-20-1	Aurora
SBI-0654331	VX-680 (Tozasertib, MK-0457)	639089-54-6	Aurora
SBI-0654340	Danusertib (PHA-739358)	827318-97-8	Aurora
SBI-0654349	Barasertib (AZD1152-HQPA)	722544-51-6	Aurora
SBI-0654350	SNS-314 Mesylate	1146618-41-8	Aurora
SBI-0654353	CYC116	693228-63-6	Aurora
SBI-0654357	ENMD-2076	1291074-87-7	Aurora
SBI-0654368	Aurora A Inhibitor I	1158838-45-9	Aurora
SBI-0654369	PHA-680632	398493-79-3	Aurora
SBI-0654376	CCT129202	942947-93-5	Aurora
SBI-0654379	Hesperadin	422513-13-1	Aurora
SBI-0800321	GSK1324726A (I-BET726)	1300031-52-0	BET
SBI-0800331	I-BRD9	1714146-59-4	BET
SBI-0800338	(+/-)-JQ1	1268524-69-1	BET
SBI-0757158	PFI-1 (PF-6405761)	1403764-72-6	BET
SBI-0757169	I-BET151 (GSK1210151A)	1300031-49-5	BET
SBI-0658003	(+)-JQ1	1268524-70-4	BET
SBI-0757166	Bromosporine	1619994-69-2	BET
SBI-0757171	I-BET-762	1260907-17-2	BET
SBI-0757176	RVX-208	1044870-39-4	BET
SBI-0757183	OTX015	202590-98-5	BET
SBI-0798104	MS-436	1395084-25-9	BET
SBI-0757191	CPI-203	1446144-04-2	BET
SBI-0800325	OF-1	919973-83-4	BRPF
SBI-0800327	NI-57	1883548-89-7	BRPF
SBI-0800336	PFI-4	900305-37-5	BRPF
SBI-0636191	Gemcitabine	95058-81-4	DNMT
SBI-0634491	5-Aza-2'-deoxycytidine	2353-33-5	DNMT
SBI-0646035	Zebularine	654065	DNMT
SBI-0050024	Azacitidine	320-67-2	DNMT
SBI-0050968	Procainamide HCl	614-39-1	DNMT
SBI-0798079	2',3',5'-triacetyl-5-Azacytidine	10302-78-0	DNMT
SBI-0055064	RG108	48208-26-0	DNMT
SBI-0757174	SGI-1027	1020149-73-8	DNMT

SBI-0798105	5-Methylcytidine	2140-61-6	DNMT
SBI-0798107	5-Methyl-2'-deoxycytidine	838-07-3	DNMT
SBI-0800323	MG149	1243583-85-8	HAT
SBI-0634482	Anacardic acid	16611-84-0	HAT
SBI-0798054	CAY10669	1243583-88-1	HAT
SBI-0646030	Garcinol	78824-30-3	HAT
SBI-0646040	Butyrolactone 3	778649-18-6	HAT
SBI-0646041	CTPB	586976-24-1	HAT
SBI-0798086	I-CBP112 (hydrochloride)	1640282-31-0	HAT
SBI-0757180	SGC-CBP30	1613695-14-9	HAT
SBI-0757186	C646	328968-36-1	HAT
SBI-0800312	Remodelin	1622921-15-6	HAT
SBI-0757155	Tubastatin A HCl	1310693-92-5	HDAC6
SBI-0757194	Tubacin	537049-40-4	HDAC6
SBI-0798111	BRD73954	1440209-96-0	HDAC6
SBI-0757156	PCI-34051	950762-95-5	HDAC8
SBI-0757172	RGFP966	1396841-57-8	HDAC-Class I
SBI-0634800	Entinostat (MS-275)	209783-80-2	HDAC-Class I
SBI-0634803	Mocetinostat (MGCD0103)	726169-73-9	HDAC-Class I
SBI-0757179	RG2833 (RGFP109)	1215493-56-3	HDAC-Class I
SBI-0647660	Romidepsin (FK228, Depsipeptide)	128517-07-7	HDAC-Class I
SBI-0798076	CBHA	174664-65-4	HDAC-Class I
SBI-0798078	Pimelic Diphenylamide 106	937039-45-7	HDAC-Class I
SBI-0053620	Sodium Butyrate	156-54-7	HDAC-Pan
SBI-0800326	4SC-202	910462-43-0	HDAC-Pan
SBI-0798099	HPOB	1429651-50-2	HDAC-Pan
SBI-0050864	Valproic acid	99-66-1	HDAC-Pan
SBI-0052872	Phenylbutyrate·Na	1716-12-7	HDAC-Pan
SBI-0053105	NSC-3852	3565-26-2	HDAC-Pan
SBI-0798047	4-iodo-SAHA	1219807-87-0	HDAC-Pan
SBI-0634430	SAHA	149647-78-9	HDAC-Pan
SBI-0634549	M-344	251456-60-7	HDAC-Pan
SBI-0757142	AR-42	935881-37-1	HDAC-Pan
SBI-0634614	Scriptaid	287383-59-9	HDAC-Pan
SBI-0757144	PCI-24781 (Abexinostat)	783355-60-2	HDAC-Pan
SBI-0757145	LAQ824 (Dacinostat)	404951-53-7	HDAC-Pan
SBI-0634799	CI-994	112522-64-2	HDAC-Pan
SBI-0757146	Quisinostat (JNJ-26481585)	875320-29-9	HDAC-Pan
SBI-0634801	BML-210	537034-17-6	HDAC-Pan
SBI-0646028	Trichostatin A	58880-19-6	HDAC-Pan
SBI-0757149	CUDC-101	1012054-59-9	HDAC-Pan
SBI-0757150	MC1568	852475-26-4	HDAC-Pan
SBI-0757151	Pracinostat (SB939)	929016-96-6	HDAC-Pan
SBI-0757152	Givinostat (ITF2357)	732302-99-7	HDAC-Pan
SBI-0646032	Apicidin	183506-66-3	HDAC-Pan

SBI-0646033	Suberoyl bis-hydroxamic acid	38937-66-5	HDAC-Pan
SBI-0646034	Nullscript	300816-11-9	HDAC-Pan
SBI-0798064	HC Toxin	83209-65-8	HDAC-Pan
SBI-0798068	coumarin-SAHA	1260635-77-5	HDAC-Pan
SBI-0798069	SAHA-BPyne	930772-88-6	HDAC-Pan
SBI-0646037	Fluoro-SAHA	149648-08-8	HDAC-Pan
SBI-0757162	Sodium Phenylbutyrate	1716-12-7	HDAC-Pan
SBI-0646038	Valproic acid hydroxamate	106132-78-9	HDAC-Pan
SBI-0646039	MC-1293	117378-93-5	HDAC-Pan
SBI-0646042	Oxamflatin	151720-43-3	HDAC-Pan
SBI-0634526	HNHA	926908-04-5	HDAC-Pan
SBI-0646045	NCH-51	848354-66-5	HDAC-Pan
SBI-0798082	Pyroxamide	382180-17-8	HDAC-Pan
SBI-0634804	Belinostat (PXD101)	414864-00-9	HDAC-Pan
SBI-0634805	Panobinostat (LBH589)	404950-80-7	HDAC-Pan
SBI-0798091	CAY10398	193551-00-7	HDAC-Pan
SBI-0798094	Chidamide	743420-02-2	HDAC-Pan
SBI-0798100	2-hexyl-4-Pentynoic Acid	96017-59-3	HDAC-Pan
SBI-0757165	Resminostat	864814-88-0	HDAC-Pan (Class I + HDAC
SBI-0798102	CAY10683	1477949-42-0	HDAC-Pan (Class I + HDAC
SBI-0646047	BML-281	1045792-66-2	HDAC-Pan (Class I + HDAC
SBI-0031029	Droxinostat	99873-43-5	HDAC-Pan (Class I + HDAC
SBI-0757157	Rocilinostat (ACY-1215)	1316214-52-4	HDAC-Pan (Class I + HDAC
SBI-0757184	Nexturastat A	1403783-31-2	HDAC-Pan (Class I + HDAC
SBI-0661466	CUDC-907	1339928-25-4	HDAC-Pan (Class I + HDAC
SBI-0654405	CYT387	1056634-68-4	JAK
SBI-0654407	Tofacitinib (CP-690550,Tasocitinib)	540737-29-9	JAK
SBI-0654431	TG101209	936091-14-4	JAK
SBI-0654448	Baricitinib (LY3009104, INCB028050)	1187594-09-7	JAK
SBI-0654455	TG101348 (SAR302503)	936091-26-8	JAK
SBI-0654480	CEP-33779	1257704-57-6	JAK
SBI-0798073	Lestaurtinib	111358-88-4	JAK
SBI-0757170	AZD1480	935666-88-9	JAK
SBI-0757177	XL019	945755-56-6	JAK
SBI-0050820	ZM 39923 HCl	1021868-92-7	JAK
SBI-0754170	Pacritinib (SB1518)	937272-79-2	JAK
SBI-0086685	WHI-P154	211555-04-3	JAK
SBI-0634628	WP1066	857064-38-1	JAK
SBI-0654261	S-Ruxolitinib (INCB018424)	941678-49-5	JAK
SBI-0654347	AT9283	896466-04-9	JAK
SBI-0757193	Filgotinib (GLPG0634)	1206161-97-8	JAK
SBI-0654389	NVP-BSK805 2HCl	1092499-93-8 (free base)	JAK
SBI-0654394	LY2784544	1229236-86-5	JAK
SBI-0654403	AZ 960	905586-69-8	JAK
SBI-0800324	ML324	1222800-79-4	KDM-JMJC/D

SBI-0798060	Daminozide	1596-84-5	KDM-JMJC/D
SBI-0798061	GSK-J1 (sodium salt)	1373422-53-7	KDM-JMJC/D
SBI-0798063	GSK-J5 (hydrochloride)	1797983-32-4	KDM-JMJC/D
SBI-0757161	GSK J4 HCl	1797983-09-5	KDM-JMJC/D
SBI-0798093	N-Oxalylglycine	5262-39-5	KDM-JMJC/D
SBI-0757188	IOX1	5852-78-8	KDM-JMJC/D
SBI-0798101	JIB-04	199596-05-9	KDM-JMJC/D
SBI-0800316	ORY-1001 (RG-6016)	1431326-61-2	KDM-LSD1
SBI-0800317	SP2509	1423715-09-6	KDM-LSD1
SBI-0757185	OG-L002	1357302-64-7	KDM-LSD1
SBI-0798109	GSK-LSD1 (hydrochloride)	1431368-48-7	KDM-LSD1
SBI-0756809	IOX2	931398-72-0	KDM-Misc
SBI-0635958	Tranylcypromine hemisulfate	13492-01-8 (H2SO4)	KDM-Misc
SBI-0646029	2,4-Pyridinedicarboxylic Acid	499-80-9	KDM-Misc
SBI-0635387	2-Hydroxyglutaric Acid (sodium salt)	40951-21-1	KDM-Misc
SBI-0757160	EPZ5676	1380288-87-8	KMT-DotL1
SBI-0757164	EPZ004777	1338466-77-5	KMT-DotL1
SBI-0757173	SGC 0946	1561178-17-3	KMT-DotL1
SBI-0800318	EI1	1418308-27-6	KMT-EZH1/2
SBI-0800320	GSK503	1346572-63-1	KMT-EZH1/2
SBI-0052994	3-Deazaneplanocin A (DZNeP)	120964-45-6	KMT-EZH1/2
SBI-0798085	GSK343	1346704-33-3	KMT-EZH1/2
SBI-0757175	EPZ-6438	1403254-99-8	KMT-EZH1/2
SBI-0798087	UNC1999	1431612-23-5	KMT-EZH1/2
SBI-0798095	EPZ005687	1396772-26-1	KMT-EZH1/2
SBI-0798103	GSK 126	1346574-57-9	KMT-EZH1/2
SBI-0800311	CPI-360	1802175-06-9	KMT-EZH1/2
SBI-0800315	CPI-169	1450655-76-1	KMT-EZH1/2
SBI-0647018	UNC0638	1255580-76-7	KMT-G9a/GLP
SBI-0800319	BRD4770	1374601-40-7	KMT-G9a/GLP
SBI-0798048	UNC0321 (trifluoroacetate salt)	1238673-32-9	KMT-G9a/GLP
SBI-0633794	BIX-01294	935693-62-2	KMT-G9a/GLP
SBI-0800334	A-366	1527503-11-2	KMT-G9a/GLP
SBI-0798070	UNC0631	1320288-19-4	KMT-G9a/GLP
SBI-0798071	UNC0646	1320288-17-2	KMT-G9a/GLP
SBI-0798080	UNC0224	1197196-48-7	KMT-G9a/GLP
SBI-0798097	UNC0642	1481677-78-4	KMT-G9a/GLP
SBI-0800330	LLY-507	1793053-37-8	KMT-Misc
SBI-0800337	A-196	1982372-88-2	KMT-Misc
SBI-0798075	Chaetocin	28097-03-2	KMT-Misc
SBI-0798110	AZ 505	1035227-43-0	KMT-Misc
SBI-0798081	Sinefungin	58944-73-3	KMT-Misc
SBI-0798098	(R)-PFI-2 (hydrochloride)	1627607-87-7	KMT-Misc
SBI-0800313	UNC0379	1620401-82-2	KMT-Misc
SBI-0757159	UPF 1069	1048371-03-4	L3MBTL

SBI-0757182	UNC669	1314241-44-5	L3MBTL
SBI-0757187	UNC1215	1415800-43-9	L3MBTL
SBI-0800322	MI-3 (Menin-MLL Inhibitor)	1271738-59-0	MLL
SBI-0798057	MI-2 (hydrochloride)	1271738-62-5	MLL
SBI-0798058	MI-nc (hydrochloride)	1359873-45-2	MLL
SBI-0798083	WDR5-0103	890190-22-4	MLL
SBI-0757178	MM-102	1417329-24-8	MLL
SBI-0754173	Olaparib (AZD2281, Ku-0059436)	763113-22-0	PARP
SBI-0757141	Veliparib (ABT-888)	912444-00-9	PARP
SBI-0757143	Iniparib (BSI-201)	160003-66-7	PARP
SBI-0757147	Rucaparib (AG-014699,PF-01367338)	459868-92-9	PARP
SBI-0757153	AG-14361	328543-09-5	PARP
SBI-0757163	AZD2461	1174043-16-3	PARP
SBI-0754156	BMN 673	1207456-01-6	PARP
SBI-0050032	INO-1001 (3-Aminobenzamide)	3544-24-9	PARP
SBI-0634597	PJ34	344458-19-1	PARP
SBI-0757181	ME0328	1445251-22-8	PARP
SBI-0757154	SGI-1776 free base	1025065-69-3	PIM
SBI-0207181	SMI-4a	438190-29-5	PIM
SBI-0757189	AZD1208	1204144-28-4	PIM
SBI-0757190	CX-6258 HCl	1353859-00-3	PIM
SBI-0800328	MS023 hydrochloride	1831110-54-3	PRMT
SBI-0800332	SGC707	1687736-54-4	PRMT
SBI-0800335	MS049 hydrochloride	1502816-23-0	PRMT
SBI-0798084	AMI-1 (sodium salt)	20324-87-2	PRMT
SBI-0051742	Ellagic Acid	476-66-4	PRMT
SBI-0050890	Piceatannol	10083-24-6	SIRTa
SBI-0051080	Resveratrol	501-36-0	SIRTa
SBI-0052275	Triacetylresveratrol	42206-94-0	SIRTa
SBI-0757148	SRT1720	1001645-58-4	SIRTa
SBI-0646044	BML-278	120533-76-8	SIRTa
SBI-0243859	CAY10591	839699-72-8	SIRTa
SBI-0646046	Aminoresveratrol sulfate	1224713-76-1	SIRTa
SBI-0046858	B2	115687-05-3	SIRTi
SBI-0051149	Suramin·6Na	129-46-4	SIRTi
SBI-0206826	Nicotinamide	98-92-0	SIRTi
SBI-0633736	BML-266	96969-83-4	SIRTi
SBI-0798052	JGB1741	1256375-38-8	SIRTi
SBI-0633793	AGK2	304896-28-4	SIRTi
SBI-0634619	EX-527	49843-98-3	SIRTi
SBI-0634621	Salermide	1105698-15-4	SIRTi
SBI-0646031	Splitomicin	1384339	SIRTi
SBI-0646043	Sirtinol	410536-97-9	SIRTi
SBI-0055128	SIRT1/2 Inhibitor IV	14513-15-6	SIRTi
SBI-0798096	AK-7	420831-40-9	SIRTi

Table 3: Epigenetic drug used for concentration curve

Compound ID	Molecule Name	CAS Number	Functional Category
SBI-0654430	TAK-901	934541-31-8	Aurora
SBI-0654442	MLN8054	869363-13-3	Aurora
SBI-0654458	MK-5108 (VX-689)	1010085-13-8	Aurora
SBI-0654253	Phthalazinone pyrazole	88048-62-7	Aurora
SBI-0646927	Alisertib (MLN8237)	1028486-01-2	Aurora
SBI-0654270	ZM 447439	331771-20-1	Aurora
SBI-0654331	VX-680 (Tozasertib, MK-0457)	639089-54-6	Aurora
SBI-0654349	Barasertib (AZD1152-HQPA)	722544-51-6	Aurora
SBI-0654350	SNS-314 Mesylate	1146618-41-8	Aurora
SBI-0654368	Aurora A Inhibitor I	1158838-45-9	Aurora
SBI-0654379	Hesperadin	422513-13-1	Aurora
SBI-0634800	Entinostat (MS-275)	209783-80-2	HDAC-Class I
SBI-0634803	Mocetinostat (MGCD0103)	726169-73-9	HDAC-Class I
SBI-0647660	Romidepsin (FK228, Depsipeptide)	128517-07-7	HDAC-Class I
SBI-0757172	RGFP966	1396841-57-8	HDAC-Class I
SBI-0757179	RG2833 (RGFP109)	1215493-56-3	HDAC-Class I
SBI-0798076	CBHA	174664-65-4	HDAC-Class I
SBI-0798078	Pimelic Diphenylamide 106	937039-45-7	HDAC-Class I
SBI-0050864	Valproic acid	99-66-1	HDAC-Pan
SBI-0053105	NSC-3852	3565-26-2	HDAC-Pan
SBI-0053620	Sodium Butyrate	156-54-7	HDAC-Pan
SBI-0634430	SAHA	149647-78-9	HDAC-Pan
SBI-0634526	HNHA	926908-04-5	HDAC-Pan
SBI-0634549	M-344	251456-60-7	HDAC-Pan
SBI-0634614	Scriptaid	287383-59-9	HDAC-Pan
SBI-0634799	CI-994	112522-64-2	HDAC-Pan
SBI-0634801	BML-210	537034-17-6	HDAC-Pan
SBI-0634804	Belinostat (PXD101)	414864-00-9	HDAC-Pan
SBI-0634805	Panobinostat (LBH589)	404950-80-7	HDAC-Pan
SBI-0646028	Trichostatin A	58880-19-6	HDAC-Pan
SBI-0646032	Apicidin	183506-66-3	HDAC-Pan
SBI-0646033	Suberoyl bis-hydroxamic acid	38937-66-5	HDAC-Pan
SBI-0646034	Nullscript	300816-11-9	HDAC-Pan
SBI-0646037	Fluoro-SAHA	149648-08-8	HDAC-Pan
SBI-0646038	Valproic acid hydroxamate	106132-78-9	HDAC-Pan
SBI-0646039	MC-1293	117378-93-5	HDAC-Pan
SBI-0646042	Oxamflatin	151720-43-3	HDAC-Pan
SBI-0646045	NCH-51	848354-66-5	HDAC-Pan
SBI-0757142	AR-42	935881-37-1	HDAC-Pan
SBI-0757144	PCI-24781 (Abexinostat)	783355-60-2	HDAC-Pan

SBI-0757145	LAQ824 (Dacinostat)	404951-53-7	HDAC-Pan
SBI-0757146	Quisinostat (JNJ-26481585)	875320-29-9	HDAC-Pan
SBI-0757149	CUDC-101	1012054-59-9	HDAC-Pan
SBI-0757150	MC1568	852475-26-4	HDAC-Pan
SBI-0757151	Pracinostat (SB939)	929016-96-6	HDAC-Pan
SBI-0757162	Sodium Phenylbutyrate	1716-12-7	HDAC-Pan
SBI-0798047	4-iodo-SAHA	1219807-87-0	HDAC-Pan
SBI-0798064	HC Toxin	83209-65-8	HDAC-Pan
SBI-0798068	coumarin-SAHA	1260635-77-5	HDAC-Pan
SBI-0798069	SAHA-BPyne	930772-88-6	HDAC-Pan
SBI-0798082	Pyroxamide	382180-17-8	HDAC-Pan
SBI-0798091	CAY10398	193551-00-7	HDAC-Pan
SBI-0798094	Chidamide	743420-02-2	HDAC-Pan
SBI-0798099	HPOB	1429651-50-2	HDAC-Pan
SBI-0798100	2-hexyl-4-Pentynoic Acid	96017-59-3	HDAC-Pan
SBI-0800326	4SC-202	910462-43-0	HDAC-Pan
SBI-0031029	Droxinostat	99873-43-5	HDAC-Pan (Class I + HDA
SBI-0646047	BML-281	1045792-66-2	HDAC-Pan (Class I + HDA
SBI-0661466	CUDC-907	1339928-25-4	HDAC-Pan (Class I + HDA
SBI-0757157	Rocilinostat (ACY-1215)	1316214-52-4	HDAC-Pan (Class I + HDA
SBI-0757165	Resminostat	864814-88-0	HDAC-Pan (Class I + HDA
SBI-0757184	Nexturastat A	1403783-31-2	HDAC-Pan (Class I + HDA
SBI-0798102	CAY10683	1477949-42-0	HDAC-Pan (Class I + HDA
SBI-0654405	CYT387	1056634-68-4	JAK
SBI-0654407	Tofacitinib (CP-690550,Tasocitinib)	540737-29-9	JAK
SBI-0654431	TG101209	936091-14-4	JAK
SBI-0654455	TG101348 (SAR302503)	936091-26-8	JAK
SBI-0654480	CEP-33779	1257704-57-6	JAK
SBI-0798073	Lestaurtinib	111358-88-4	JAK
SBI-0757170	AZD1480	935666-88-9	JAK
SBI-0757177	XL019	945755-56-6	JAK
SBI-0050820	ZM 39923 HCl	1021868-92-7	JAK
SBI-0754170	Pacritinib (SB1518)	937272-79-2	JAK
SBI-0634628	WP1066	857064-38-1	JAK
SBI-0654347	AT9283	896466-04-9	JAK
SBI-0654389	NVP-BSK805 2HCl	1092499-93-8 (free base)	JAK
SBI-0654394	LY2784544	1229236-86-5	JAK
SBI-0654403	AZ 960	905586-69-8	JAK
SBI-0800318	EI1	1418308-27-6	KMT-EZH1/2
SBI-0798085	GSK343	1346704-33-3	KMT-EZH1/2
SBI-0798087	UNC1999	1431612-23-5	KMT-EZH1/2
SBI-0798103	GSK 126	1346574-57-9	KMT-EZH1/2
SBI-0800311	CPI-360	1802175-06-9	KMT-EZH1/2
SBI-0800315	CPI-169	1450655-76-1	KMT-EZH1/2
SBI-0046858	B2	115687-05-3	SIRTi

SBI-0051149	Suramin·6Na	129-46-4	SIRTi
SBI-0633736	BML-266	96969-83-4	SIRTi
SBI-0646031	Splitomicin	1384339	SIRTi
SBI-0646043	Sirtinol	410536-97-9	SIRTi
SBI-0055128	SIRT1/2 Inhibitor IV	14513-15-6	SIRTi
SBI-0798096	AK-7	420831-40-9	SIRTi

Compound ID	Molecule Name	CAS Number	Functional Category	Concentra
SBI-0757155	Tubastatin A HCl	1310693-92-5	HDAC6	10
SBI-0757194	Tubacin	537049-40-4	HDAC6	10
SBI-0798111	BRD73954	1440209-96-0	HDAC6	10
SBI-0757156	PCI-34051	950762-95-5	HDAC8	10
SBI-0634800	Entinostat (MS-275)	209783-80-2	HDAC-Class I	1
SBI-0634803	Mocetinostat (MGCD0103)	726169-73-9	HDAC-Class I	1
SBI-0757172	RGFP966	1396841-57-8	HDAC-Class I	3
SBI-0757179	RG2833 (RGFP109)	1215493-56-3	HDAC-Class I	1
SBI-0798076	CBHA	174664-65-4	HDAC-Class I	1
SBI-0798078	Pimelic Diphenylamide 106	937039-45-7	HDAC-Class I	1
SBI-0050864	Valproic acid	99-66-1	HDAC-Pan	10
SBI-0053105	NSC-3852	3565-26-2	HDAC-Pan	1
SBI-0634430	SAHA	149647-78-9	HDAC-Pan	1
SBI-0634614	Scriptaid	287383-59-9	HDAC-Pan	1
SBI-0634799	CI-994	112522-64-2	HDAC-Pan	3
SBI-0634801	BML-210	537034-17-6	HDAC-Pan	10
SBI-0646028	Trichostatin A	58880-19-6	HDAC-Pan	1
SBI-0646033	Suberoyl bis-hydroxamic acid	38937-66-5	HDAC-Pan	10
SBI-0646034	Nullscript	300816-11-9	HDAC-Pan	3
SBI-0798069	SAHA-BPyne	930772-88-6	HDAC-Pan	10
SBI-0798082	Pyroxamide	382180-17-8	HDAC-Pan	3
SBI-0798091	CAY10398	193551-00-7	HDAC-Pan	1
SBI-0798094	Chidamide	743420-02-2	HDAC-Pan	3
SBI-0798099	HPOB	1429651-50-2	HDAC-Pan	10
SBI-0800326	4SC-202	910462-43-0	HDAC-Pan	1
SBI-0031029	Droxinostat	99873-43-5	HDAC-Pan (Class I + HDAC6)	1
SBI-0646047	BML-281	1045792-66-2	HDAC-Pan (Class I + HDAC6)	1
SBI-0757157	Rocilinostat (ACY-1215)	1316214-52-4	HDAC-Pan (Class I + HDAC6)	1
SBI-0757165	Resminostat	864814-88-0	HDAC-Pan (Class I + HDAC6)	1
SBI-0757184	Nexturastat A	1403783-31-2	HDAC-Pan (Class I + HDAC6)	1
SBI-0052994	3-Deazaneplanocin A (DZNeP)	120964-45-6	KMT-EZH1/2	1
SBI-0757175	EPZ-6438	1403254-99-8	KMT-EZH1/2	1
SBI-0798085	GSK343	1346704-33-3	KMT-EZH1/2	1
SBI-0798087	UNC1999	1431612-23-5	KMT-EZH1/2	1
SBI-0798103	GSK 126	1346574-57-9	KMT-EZH1/2	1
SBI-0800311	CPI-360	1802175-06-9	KMT-EZH1/2	1
SBI-0800315	CPI-169	1450655-76-1	KMT-EZH1/2	1
SBI-0800318	EI1	1418308-27-6	KMT-EZH1/2	1
SBI-0800320	GSK503	1346572-63-1	KMT-EZH1/2	1
SBI-0633794	BIX-01294	935693-62-2	KMT-G9a/GLP	3
SBI-0647018	UNC0638	1255580-76-7	KMT-G9a/GLP	3
SBI-0798070	UNC0631	1320288-19-4	KMT-G9a/GLP	3
SBI-0798071	UNC0646	1320288-17-2	KMT-G9a/GLP	3
SBI-0798080	UNC0224	1197196-48-7	KMT-G9a/GLP	3

SBI-0798097	UNC0642	1481677-78-4	KMT-G9a/GLP	3
SBI-0798081	Sinefungin	58944-73-3	KMT-Misc	10
SBI-0798098	(R)-PFI-2 (hydrochloride)	1627607-87-7	KMT-Misc	10
SBI-0800313	UNC0379	1620401-82-2	KMT-Misc	1
SBI-0798110	AZ 505	1035227-43-0	KMT-Misc	10
SBI-0800330	LLY-507	1793053-37-8	KMT-Misc	1
SBI-0046858	B2	115687-05-3	SIRTi	1
SBI-0051149	Suramin·6Na	129-46-4	SIRTi	3
SBI-0055128	SIRT1/2 Inhibitor IV	14513-15-6	SIRTi	10
SBI-0633736	BML-266	96969-83-4	SIRTi	3
SBI-0646043	Sirtinol	410536-97-9	SIRTi	3
SBI-0798096	AK-7	420831-40-9	SIRTi	10

Table 5: Epigenetic drug screened for sensitization to cytotoxic treatment

Compound ID	Molecule Name	CAS Number	Functional Category
SBI-0654369	PHA-680632	398493-79-3	Aurora
SBI-0654442	MLN8054	869363-13-3	Aurora
SBI-0654340	Danusertib (PHA-739358)	827318-97-8	Aurora
SBI-0654350	SNS-314 Mesylate	1146618-41-8	Aurora
SBI-0654376	CCT129202	942947-93-5	Aurora
SBI-0654331	VX-680 (Tozasertib, MK-0457)	639089-54-6	Aurora
SBI-0654432	AMG-900	945595-80-2	Aurora
SBI-0654357	ENMD-2076	1291074-87-7	Aurora
SBI-0654368	Aurora A Inhibitor I	1158838-45-9	Aurora
SBI-0646927	Alisertib (MLN8237)	1028486-01-2	Aurora
SBI-0654430	TAK-901	934541-31-8	Aurora
SBI-0654349	Barasertib (AZD1152-HQPA)	722544-51-6	Aurora
SBI-0086733	JNJ-7706621	443797-96-4	Aurora
SBI-0654458	MK-5108 (VX-689)	1010085-13-8	Aurora
SBI-0654353	CYC116	693228-63-6	Aurora
SBI-0654379	Hesperadin	422513-13-1	Aurora
SBI-0654463	CCT137690	1095382-05-0	Aurora
SBI-0654270	ZM 447439	331771-20-1	Aurora
SBI-0654253	Phthalazinone pyrazole	88048-62-7	Aurora
SBI-0757183	OTX015	202590-98-5	BET
SBI-0757169	I-BET151 (GSK1210151A)	1300031-49-5	BET
SBI-0658003	(+)-JQ1	1268524-70-4	BET
SBI-0800321	GSK1324726A (I-BET726)	1300031-52-0	BET
SBI-0757191	CPI-203	1446144-04-2	BET
SBI-0798104	MS-436	1395084-25-9	BET
SBI-0757158	PFI-1 (PF-6405761)	1403764-72-6	BET
SBI-0757171	I-BET-762	1260907-17-2	BET
SBI-0800331	I-BRD9	1714146-59-4	BET
SBI-0800338	(+/-)-JQ1	1268524-69-1	BET
SBI-0757176	RVX-208	1044870-39-4	BET
SBI-0757166	Bromosporine	1619994-69-2	BET
SBI-0800336	PFI-4	900305-37-5	BRPF
SBI-0800327	NI-57	1883548-89-7	BRPF
SBI-0800325	OF-1	919973-83-4	BRPF
SBI-0634491	5-Aza-2'-deoxycytidine	2353-33-5	DNMT
SBI-0798107	5-Methyl-2'-deoxycytidine	838-07-3	DNMT
SBI-0636191	Gemcitabine	95058-81-4	DNMT
SBI-0646035	Zebularine	654065	DNMT
SBI-0757174	SGI-1027	1020149-73-8	DNMT
SBI-0050024	Azacitidine	320-67-2	DNMT
SBI-0798105	5-Methylcytidine	2140-61-6	DNMT
SBI-0055064	RG108	48208-26-0	DNMT

SBI-0050968	Procainamide HCl	614-39-1	DNMT
SBI-0798079	2',3',5'-triacetyl-5-Azacytidine	10302-78-0	DNMT
SBI-0800312	Remodelin	1622921-15-6	HAT
SBI-0757180	SGC-CBP30	1613695-14-9	HAT
SBI-0800323	MG149	1243583-85-8	HAT
SBI-0646040	Butyrolactone 3	778649-18-6	HAT
SBI-0798054	CAY10669	1243583-88-1	HAT
SBI-0757186	C646	328968-36-1	HAT
SBI-0634482	Anacardic acid	16611-84-0	HAT
SBI-0798086	I-CBP112 (hydrochloride)	1640282-31-0	HAT
SBI-0646041	CTPB	586976-24-1	HAT
SBI-0646030	Garcinol	78824-30-3	HAT
SBI-0757155	Tubastatin A HCl	1310693-92-5	HDAC6
SBI-0798111	BRD73954	1440209-96-0	HDAC6
SBI-0757194	Tubacin	537049-40-4	HDAC6
SBI-0757156	PCI-34051	950762-95-5	HDAC8
SBI-0634803	Mocetinostat (MGCD0103)	726169-73-9	HDAC-Class I
SBI-0647660	Romidepsin (FK228, Depsipeptide)	128517-07-7	HDAC-Class I
SBI-0798076	CBHA	174664-65-4	HDAC-Class I
SBI-0634800	Entinostat (MS-275)	209783-80-2	HDAC-Class I
SBI-0757179	RG2833 (RGFP109)	1215493-56-3	HDAC-Class I
SBI-0757172	RGFP966	1396841-57-8	HDAC-Class I
SBI-0798078	Pimelic Diphenylamide 106	937039-45-7	HDAC-Class I
SBI-0798068	coumarin-SAHA	1260635-77-5	HDAC-Pan
SBI-0757142	AR-42	935881-37-1	HDAC-Pan
SBI-0634614	Scriptaid	287383-59-9	HDAC-Pan
SBI-0798094	Chidamide	743420-02-2	HDAC-Pan
SBI-0634805	Panobinostat (LBH589)	404950-80-7	HDAC-Pan
SBI-0634430	SAHA	149647-78-9	HDAC-Pan
SBI-0757145	LAQ824 (Dacinostat)	404951-53-7	HDAC-Pan
SBI-0757149	CUDC-101	1012054-59-9	HDAC-Pan
SBI-0798091	CAY10398	193551-00-7	HDAC-Pan
SBI-0798047	4-iodo-SAHA	1219807-87-0	HDAC-Pan
SBI-0757146	Quisinostat (JNJ-26481585)	875320-29-9	HDAC-Pan
SBI-0757151	Pracinostat (SB939)	929016-96-6	HDAC-Pan
SBI-0800326	4SC-202	910462-43-0	HDAC-Pan
SBI-0646042	Oxamflatin	151720-43-3	HDAC-Pan
SBI-0053105	NSC-3852	3565-26-2	HDAC-Pan
SBI-0757144	PCI-24781 (Abexinostat)	783355-60-2	HDAC-Pan
SBI-0634804	Belinostat (PXD101)	414864-00-9	HDAC-Pan
SBI-0646032	Apicidin	183506-66-3	HDAC-Pan
SBI-0798082	Pyroxamide	382180-17-8	HDAC-Pan
SBI-0634549	M-344	251456-60-7	HDAC-Pan
SBI-0646028	Trichostatin A	58880-19-6	HDAC-Pan
SBI-0757152	Givinostat (ITF2357)	732302-99-7	HDAC-Pan

SBI-0798064	HC Toxin	83209-65-8	HDAC-Pan
SBI-0646037	Fluoro-SAHA	149648-08-8	HDAC-Pan
SBI-0798099	HPOB	1429651-50-2	HDAC-Pan
SBI-0757162	Sodium Phenylbutyrate	1716-12-7	HDAC-Pan
SBI-0646033	Suberoyl bis-hydroxamic acid	38937-66-5	HDAC-Pan
SBI-0646034	Nullscript	300816-11-9	HDAC-Pan
SBI-0646045	NCH-51	848354-66-5	HDAC-Pan
SBI-0050864	Valproic acid	99-66-1	HDAC-Pan
SBI-0052872	Phenylbutyrate·Na	1716-12-7	HDAC-Pan
SBI-0757150	MC1568	852475-26-4	HDAC-Pan
SBI-0634801	BML-210	537034-17-6	HDAC-Pan
SBI-0634526	HNHA	926908-04-5	HDAC-Pan
SBI-0053620	Sodium Butyrate	156-54-7	HDAC-Pan
SBI-0798100	2-hexyl-4-Pentynoic Acid	96017-59-3	HDAC-Pan
SBI-0798069	SAHA-BPyne	930772-88-6	HDAC-Pan
SBI-0634799	CI-994	112522-64-2	HDAC-Pan
SBI-0646038	Valproic acid hydroxamate	106132-78-9	HDAC-Pan
SBI-0646039	MC-1293	117378-93-5	HDAC-Pan
SBI-0031029	Droxinostat	99873-43-5	HDAC-Pan (Class I + HDA
SBI-0757157	Rocilinostat (ACY-1215)	1316214-52-4	HDAC-Pan (Class I + HDA
SBI-0661466	CUDC-907	1339928-25-4	HDAC-Pan (Class I + HDA
SBI-0646047	BML-281	1045792-66-2	HDAC-Pan (Class I + HDA
SBI-0757165	Resminostat	864814-88-0	HDAC-Pan (Class I + HDA
SBI-0757184	Nexturastat A	1403783-31-2	HDAC-Pan (Class I + HDA
SBI-0798102	CAY10683	1477949-42-0	HDAC-Pan (Class I + HDA
SBI-0798073	Lestaurtinib	111358-88-4	JAK
SBI-0654347	AT9283	896466-04-9	JAK
SBI-0654394	LY2784544	1229236-86-5	JAK
SBI-0654431	TG101209	936091-14-4	JAK
SBI-0754170	Pacritinib (SB1518)	937272-79-2	JAK
SBI-0654455	TG101348 (SAR302503)	936091-26-8	JAK
SBI-0654405	CYT387	1056634-68-4	JAK
SBI-0654403	AZ 960	905586-69-8	JAK
SBI-0757170	AZD1480	935666-88-9	JAK
SBI-0634628	WP1066	857064-38-1	JAK
SBI-0050820	ZM 39923 HCl	1021868-92-7	JAK
SBI-0757193	Filgotinib (GLPG0634)	1206161-97-8	JAK
SBI-0654261	S-Ruxolitinib (INCB018424)	941678-49-5	JAK
SBI-0654480	CEP-33779	1257704-57-6	JAK
SBI-0654407	Tofacitinib (CP-690550,Tasocitinib)	540737-29-9	JAK
SBI-0757177	XL019	945755-56-6	JAK
SBI-0086685	WHI-P154	211555-04-3	JAK
SBI-0654389	NVP-BSK805 2HCl	1092499-93-8 (free base)	JAK
SBI-0654448	Baricitinib (LY3009104, INCB028050)	1187594-09-7	JAK
SBI-0798063	GSK-J5 (hydrochloride)	1797983-32-4	KDM-JMJC/D

SBI-0798061	GSK-J1 (sodium salt)	1373422-53-7	KDM-JMJC/D
SBI-0798060	Daminozide	1596-84-5	KDM-JMJC/D
SBI-0757188	IOX1	5852-78-8	KDM-JMJC/D
SBI-0757161	GSK J4 HCl	1797983-09-5	KDM-JMJC/D
SBI-0798093	N-Oxalylglycine	5262-39-5	KDM-JMJC/D
SBI-0800324	ML324	1222800-79-4	KDM-JMJC/D
SBI-0798101	JIB-04	199596-05-9	KDM-JMJC/D
SBI-0800317	SP2509	1423715-09-6	KDM-LSD1
SBI-0798109	GSK-LSD1 (hydrochloride)	1431368-48-7	KDM-LSD1
SBI-0800316	ORY-1001 (RG-6016)	1431326-61-2	KDM-LSD1
SBI-0757185	OG-L002	1357302-64-7	KDM-LSD1
SBI-0635387	2-Hydroxyglutaric Acid (sodium salt)	40951-21-1	KDM-Misc
SBI-0756809	IOX2	931398-72-0	KDM-Misc
SBI-0635958	Tranylcypromine hemisulfate	13492-01-8 (H2SO4)	KDM-Misc
SBI-0646029	2,4-Pyridinedicarboxylic Acid	499-80-9	KDM-Misc
SBI-0757160	EPZ5676	1380288-87-8	KMT-DotL1
SBI-0757173	SGC 0946	1561178-17-3	KMT-DotL1
SBI-0757164	EPZ004777	1338466-77-5	KMT-DotL1
SBI-0800315	CPI-169	1450655-76-1	KMT-EZH1/2
SBI-0052994	3-Deazaneplanocin A (DZNeP)	120964-45-6	KMT-EZH1/2
SBI-0800311	CPI-360	1802175-06-9	KMT-EZH1/2
SBI-0798087	UNC1999	1431612-23-5	KMT-EZH1/2
SBI-0757175	EPZ-6438	1403254-99-8	KMT-EZH1/2
SBI-0798095	EPZ005687	1396772-26-1	KMT-EZH1/2
SBI-0800318	EI1	1418308-27-6	KMT-EZH1/2
SBI-0798103	GSK 126	1346574-57-9	KMT-EZH1/2
SBI-0800320	GSK503	1346572-63-1	KMT-EZH1/2
SBI-0798085	GSK343	1346704-33-3	KMT-EZH1/2
SBI-0647018	UNC0638	1255580-76-7	KMT-G9a/GLP
SBI-0633794	BIX-01294	935693-62-2	KMT-G9a/GLP
SBI-0798071	UNC0646	1320288-17-2	KMT-G9a/GLP
SBI-0798097	UNC0642	1481677-78-4	KMT-G9a/GLP
SBI-0800319	BRD4770	1374601-40-7	KMT-G9a/GLP
SBI-0798070	UNC0631	1320288-19-4	KMT-G9a/GLP
SBI-0798048	UNC0321 (trifluoroacetate salt)	1238673-32-9	KMT-G9a/GLP
SBI-0798080	UNC0224	1197196-48-7	KMT-G9a/GLP
SBI-0800334	A-366	1527503-11-2	KMT-G9a/GLP
SBI-0798075	Chaetocin	28097-03-2	KMT-Misc
SBI-0800313	UNC0379	1620401-82-2	KMT-Misc
SBI-0798081	Sinefungin	58944-73-3	KMT-Misc
SBI-0800330	LLY-507	1793053-37-8	KMT-Misc
SBI-0798098	(R)-PFI-2 (hydrochloride)	1627607-87-7	KMT-Misc
SBI-0800337	A-196	1982372-88-2	KMT-Misc
SBI-0798110	AZ 505	1035227-43-0	KMT-Misc
SBI-0757187	UNC1215	1415800-43-9	L3MBTL

SBI-0757182	UNC669	1314241-44-5	L3MBTL
SBI-0757159	UPF 1069	1048371-03-4	L3MBTL
SBI-0757167	Lomeguatrib	192441-08-0	MGMT
SBI-0798057	MI-2 (hydrochloride)	1271738-62-5	MLL
SBI-0800322	MI-3 (Menin-MLL Inhibitor)	1271738-59-0	MLL
SBI-0757178	MM-102	1417329-24-8	MLL
SBI-0798058	MI-nc (hydrochloride)	1359873-45-2	MLL
SBI-0798083	WDR5-0103	890190-22-4	MLL
SBI-0754173	Olaparib (AZD2281, Ku-0059436)	763113-22-0	PARP
SBI-0754156	BMN 673	1207456-01-6	PARP
SBI-0050032	INO-1001 (3-Aminobenzamide)	3544-24-9	PARP
SBI-0757143	Iniparib (BSI-201)	160003-66-7	PARP
SBI-0634597	PJ34	344458-19-1	PARP
SBI-0757163	AZD2461	1174043-16-3	PARP
SBI-0757181	ME0328	1445251-22-8	PARP
SBI-0757141	Veliparib (ABT-888)	912444-00-9	PARP
SBI-0757153	AG-14361	328543-09-5	PARP
SBI-0757147	Rucaparib (AG-014699,PF-01367338)	459868-92-9	PARP
SBI-0757154	SGI-1776 free base	1025065-69-3	PIM
SBI-0757190	CX-6258 HCl	1353859-00-3	PIM
SBI-0207181	SMI-4a	438190-29-5	PIM
SBI-0757189	AZD1208	1204144-28-4	PIM
SBI-0051742	Ellagic Acid	476-66-4	PRMT
SBI-0798084	AMI-1 (sodium salt)	20324-87-2	PRMT
SBI-0800328	MS023 hydrochloride	1831110-54-3	PRMT
SBI-0800335	MS049 hydrochloride	1502816-23-0	PRMT
SBI-0800332	SGC707	1687736-54-4	PRMT
SBI-0051080	Resveratrol	501-36-0	SIRTa
SBI-0757148	SRT1720	1001645-58-4	SIRTa
SBI-0646046	Aminoresveratrol sulfate	1224713-76-1	SIRTa
SBI-0243859	CAY10591	839699-72-8	SIRTa
SBI-0646044	BML-278	120533-76-8	SIRTa
SBI-0052275	Triacetylresveratrol	42206-94-0	SIRTa
SBI-0050890	Piceatannol	10083-24-6	SIRTa
SBI-0046858	B2	115687-05-3	SIRTi
SBI-0798096	AK-7	420831-40-9	SIRTi
SBI-0051149	Suramin·6Na	129-46-4	SIRTi
SBI-0646031	Splitomicin	1384339	SIRTi
SBI-0646043	Sirtinol	410536-97-9	SIRTi
SBI-0633736	BML-266	96969-83-4	SIRTi
SBI-0634621	Salermide	1105698-15-4	SIRTi
SBI-0055128	SIRT1/2 Inhibitor IV	14513-15-6	SIRTi
SBI-0634619	EX-527	49843-98-3	SIRTi
SBI-0206826	Nicotinamide	98-92-0	SIRTi
SBI-0798052	JGB1741	1256375-38-8	SIRTi

SBI-0633793	AGK2	304896-28-4	SIRTi

Reference:

1. Farhy C, Hariharan S, Ylanko J, van Woudenberg L, Cimadamore F, Ugarte F, Forsberg C, Huang C-T, Andrews D, Terskikh A. Multiparametric Signature of Glioblastoma Differentiation Revealed by Imaging of Cellular Epigenetic Landscapes. bioRxiv. 2018. doi: 10.1101/348888.

2. Jenuwein T, Allis CD. Translating the histone code. Science. 2001;293(5532):1074-80. doi: 10.1126/science.1063127. PubMed PMID: 11498575.

3. Lawrence M, Daujat S, Schneider R. Lateral Thinking: How Histone Modifications Regulate Gene Expression. Trends Genet. 2016;32(1):42-56. doi: 10.1016/j.tig.2015.10.007. PubMed PMID: 26704082.

4. Jones PA, Issa JP, Baylin S. Targeting the cancer epigenome for therapy. Nat Rev Genet. 2016;17(10):630-41. doi: 10.1038/nrg.2016.93. PubMed PMID: 27629931.

5. Mann BS, Johnson JR, Cohen MH, Justice R, Pazdur R. FDA approval summary: vorinostat for treatment of advanced primary cutaneous T-cell lymphoma. Oncologist. 2007;12(10):1247-52. doi: 10.1634/theoncologist.12-10-1247. PubMed PMID: 17962618.

6. Kaminskas E, Farrell AT, Wang YC, Sridhara R, Pazdur R. FDA drug approval summary: azacitidine (5-azacytidine, Vidaza) for injectable suspension. Oncologist. 2005;10(3):176-82. doi: 10.1634/theoncologist.10-3-176. PubMed PMID: 15793220.

7. Muka T, Koromani F, Portilla E, O'Connor A, Bramer WM, Troup J, Chowdhury R, Dehghan A, Franco OH. The role of epigenetic modifications in cardiovascular disease: A systematic review. Int J Cardiol. 2016;212:174-83. doi: 10.1016/j.ijcard.2016.03.062. PubMed PMID: 27038728.

8. Graff J, Rei D, Guan JS, Wang WY, Seo J, Hennig KM, Nieland TJ, Fass DM, Kao PF, Kahn M, Su SC, Samiei A, Joseph N, Haggarty SJ, Delalle I, Tsai LH. An epigenetic blockade of cognitive functions in the neurodegenerating brain. Nature. 2012;483(7388):222-6. doi: 10.1038/nature10849. PubMed PMID: 22388814; PMCID: PMC3498952.

9. Falkenberg KJ, Johnstone RW. Histone deacetylases and their inhibitors in cancer, neurological diseases and immune disorders. Nat Rev Drug Discov. 2014;13(9):673-91. doi: 10.1038/nrd4360. PubMed PMID: 25131830.

10. Martinez NJ, Simeonov A. Cell-based assays to support the profiling of small molecules with histone methyltransferase and demethylase modulatory activity. Drug Discov Today Technol. 2015;18:9-17. doi: 10.1016/j.ddtec.2015.10.004. PubMed PMID: 26723887; PMCID: PMC4698313.

11. Gul S. Epigenetic assays for chemical biology and drug discovery. Clin Epigenetics. 2017;9:41. doi: 10.1186/s13148-017-0342-6. PubMed PMID: 28439316; PMCID: PMC5399855.

12. Campbell RM, Tummino PJ. Cancer epigenetics drug discovery and development: the challenge of hitting the mark. J Clin Invest. 2014;124(1):64-9. doi: 10.1172/JCI71605. PubMed PMID: 24382391; PMCID: PMC3871251.

13. Quinn AM, Simeonov A. Methods for Activity Analysis of the Proteins that Regulate Histone Methylation. Curr Chem Genomics. 2011;5(Suppl 1):95-105. doi: 10.2174/1875397301005010095. PubMed PMID: 21966349; PMCID: PMC3180180.

14. Moore K, Rees S. Cell-based versus isolated target screening: how lucky do you feel? J Biomol Screen. 2001;6(2):69-74. doi: 10.1177/108705710100600202. PubMed PMID: 11689100.

15. St Pierre R, Kadoch C. Mammalian SWI/SNF complexes in cancer: emerging therapeutic opportunities. Curr Opin Genet Dev. 2017;42:56-67. doi: 10.1016/j.gde.2017.02.004. PubMed PMID: 28391084; PMCID: PMC5777332.

16. Holoch D, Margueron R. Mechanisms Regulating PRC2 Recruitment and Enzymatic Activity. Trends Biochem Sci. 2017;42(7):531-42. doi: 10.1016/j.tibs.2017.04.003. PubMed PMID: 28483375.

17. Shema E, Jones D, Shoresh N, Donohue L, Ram O, Bernstein BE. Single-molecule decoding of combinatorially modified nucleosomes. Science. 2016;352(6286):717-21. doi: 10.1126/science.aad7701. PubMed PMID: 27151869; PMCID: PMC4904710.

18. Bernstein E, Duncan EM, Masui O, Gil J, Heard E, Allis CD. Mouse polycomb proteins bind differentially to methylated histone H3 and RNA and are enriched in facultative heterochromatin. Mol Cell Biol. 2006;26(7):2560-9. Epub 2006/03/16. doi: 26/7/2560 [pii]

10.1128/MCB.26.7.2560-2569.2006. PubMed PMID: 16537902; PMCID: 1430336.

19. Hughes JP, Rees S, Kalindjian SB, Philpott KL. Principles of early drug discovery. Br J Pharmacol. 2011;162(6):1239-49. doi: 10.1111/j.1476-5381.2010.01127.x. PubMed PMID: 21091654; PMCID: PMC3058157.

20. Kang J, Hsu CH, Wu Q, Liu S, Coster AD, Posner BA, Altschuler SJ, Wu LF. Improving drug discovery with high-content phenotypic screens by systematic selection of reporter cell lines. Nat Biotechnol. 2016;34(1):70-7. doi: 10.1038/nbt.3419. PubMed PMID: 26655497; PMCID: PMC4844861.

21. Scheeder C, Heigwer F, Boutros M. Machine learning and image-based profiling in drug discovery. Curr Opin Syst Biol. 2018;10:43-52. doi: 10.1016/j.coisb.2018.05.004. PubMed PMID: 30159406; PMCID: PMC6109111.

22. Dang L, White DW, Gross S, Bennett BD, Bittinger MA, Driggers EM, Fantin VR, Jang HG, Jin S, Keenan MC, Marks KM, Prins RM, Ward PS, Yen KE, Liau LM, Rabinowitz JD, Cantley LC, Thompson CB, Vander Heiden MG, Su SM. Cancer-associated IDH1 mutations produce 2-hydroxyglutarate. Nature. 2010;465(7300):966. doi: 10.1038/nature09132. PubMed PMID: 20559394; PMCID: PMC3766976.

23. Liu A, Hou C, Chen H, Zong X, Zong P. Genetics and Epigenetics of Glioblastoma: Applications and Overall Incidence of IDH1 Mutation. Front Oncol. 2016;6:16. doi: 10.3389/fonc.2016.00016. PubMed PMID: 26858939; PMCID: PMC4731485.

24. Esteller M, Garcia-Foncillas J, Andion E, Goodman SN, Hidalgo OF, Vanaclocha V, Baylin SB, Herman JG. Inactivation of the DNA-repair gene MGMT and the clinical response of gliomas to alkylating agents. N Engl J Med. 2000;343(19):1350-4. doi: 10.1056/NEJM200011093431901. PubMed PMID: 11070098.

25. Collins TJ, Ylanko J, Geng F, Andrews DW. A Versatile Cell Death Screening Assay Using Dye-Stained Cells and Multivariate Image Analysis. Assay Drug Dev Technol. 2015;13(9):547-57. doi: 10.1089/adt.2015.661. PubMed PMID: 26422066; PMCID: PMC4652219.

26. Creyghton MP, Cheng AW, Welstead GG, Kooistra T, Carey BW, Steine EJ, Hanna J, Lodato MA, Frampton GM, Sharp PA, Boyer LA, Young RA, Jaenisch R. Histone H3K27ac separates active from poised enhancers and predicts developmental state. Proc Natl Acad Sci U S A. 2010;107(50):21931-6. Epub 2010/11/26. doi: 10.1073/pnas.1016071107. PubMed PMID: 21106759; PMCID: 3003124.

27. Shlyueva D, Stampfel G, Stark A. Transcriptional enhancers: from properties to genome-wide predictions. Nat Rev Genet. 2014;15(4):272-86. doi: 10.1038/nrg3682. PubMed PMID: 24614317.

28. Haralick RM, Shanmugam K. Textural features for image classification. IEEE Transactions on systems, man, and cybernetics. 1973(6):610-21.

29. Hamilton NA, Pantelic RS, Hanson K, Teasdale RD. Fast automated cell phenotype image classification. BMC Bioinformatics. 2007;8:110. doi: 10.1186/1471-2105-8-110. PubMed PMID: 17394669; PMCID: PMC1847687.

30. Loo LH, Lin HJ, Steininger RJ, 3rd, Wang Y, Wu LF, Altschuler SJ. An approach for extensibly profiling the molecular states of cellular subpopulations. Nat Methods. 2009;6(10):759-65. doi: 10.1038/nmeth.1375. PubMed PMID: 19767759; PMCID: PMC2818727.

31. Caie PD, Walls RE, Ingleston-Orme A, Daya S, Houslay T, Eagle R, Roberts ME, Carragher NO. High-content phenotypic profiling of drug response signatures across distinct cancer cells. Mol Cancer Ther. 2010;9(6):1913-26. doi: 10.1158/1535-7163.MCT-09-1148. PubMed PMID: 20530715.

32. Gustafsdottir SM, Ljosa V, Sokolnicki KL, Anthony Wilson J, Walpita D, Kemp MM, Petri Seiler K, Carrel HA, Golub TR, Schreiber SL, Clemons PA, Carpenter AE, Shamji AF. Multiplex cytological profiling assay to measure diverse cellular states. PLoS One. 2013;8(12):e80999. doi: 10.1371/journal.pone.0080999. PubMed PMID: 24312513; PMCID: PMC3847047.

33. Loo LH, Wu LF, Altschuler SJ. Image-based multivariate profiling of drug responses from single cells. Nat Methods. 2007;4(5):445-53. doi: 10.1038/nmeth1032. PubMed PMID: 17401369.

34. Sayegh J, Cao J, Zou MR, Morales A, Blair LP, Norcia M, Hoyer D, Tackett AJ, Merkel JS, Yan Q. Identification of small molecule inhibitors of Jumonji AT-rich interactive domain 1B (JARID1B) histone demethylase by a sensitive high throughput screen. J Biol Chem. 2013;288(13):9408-17. doi: 10.1074/jbc.M112.419861. PubMed PMID: 23408432; PMCID: PMC3611010.

35. Luense S, Denner P, Fernandez-Montalvan A, Hartung I, Husemann M, Stresemann C, Prechtl S. Quantification of histone H3 Lys27 trimethylation (H3K27me3) by high-throughput microscopy enables cellular large-scale screening for small-molecule EZH2 inhibitors. J Biomol Screen. 2015;20(2):190-201. doi: 10.1177/1087057114559668. PubMed PMID: 25409661; PMCID: PMC4361481.

36. Peterson GM, Naunton M. Valproate: a simple chemical with so much to offer. J Clin Pharm Ther. 2005;30(5):417-21. doi: 10.1111/j.1365-2710.2005.00671.x. PubMed PMID: 16164485.

37. Phiel CJ, Zhang F, Huang EY, Guenther MG, Lazar MA, Klein PS. Histone deacetylase is a direct target of valproic acid, a potent anticonvulsant, mood stabilizer, and teratogen. J Biol Chem. 2001;276(39):36734-41. doi: 10.1074/jbc.M101287200. PubMed PMID: 11473107.

38. Shapiro JR, Yung WK, Shapiro WR. Isolation, karyotype, and clonal growth of heterogeneous subpopulations of human malignant gliomas. Cancer Res. 1981;41(6):2349-59. PubMed PMID: 7016313.

39. Puchalski RB, Shah N, Miller J, Dalley R, Nomura SR, Yoon JG, Smith KA, Lankerovich M, Bertagnolli D, Bickley K, Boe AF, Brouner K, Butler S, Caldejon S, Chapin M, Datta S, Dee N, Desta T, Dolbeare T, Dotson N, Ebbert A, Feng D, Feng X, Fisher M, Gee G, Goldy J, Gourley L, Gregor BW, Gu G, Hejazinia N, Hohmann J, Hothi P, Howard R, Joines K, Kriedberg A, Kuan L, Lau C, Lee F, Lee H, Lemon T, Long F, Mastan N, Mott E, Murthy C, Ngo K, Olson E, Reding M, Riley Z, Rosen D, Sandman D, Shapovalova N, Slaughterbeck CR, Sodt A, Stockdale G, Szafer A, Wakeman W, Wohnoutka PE, White SJ, Marsh D, Rostomily RC, Ng L, Dang C, Jones A, Keogh B, Gittleman HR, Barnholtz-Sloan JS, Cimino PJ, Uppin MS, Keene CD, Farrokhi FR, Lathia JD, Berens ME, Iavarone A, Bernard A, Lein E, Phillips JW, Rostad SW, Cobbs C, Hawrylycz MJ, Foltz GD. An anatomic transcriptional atlas of human glioblastoma. Science. 2018;360(6389):660-3. doi: 10.1126/science.aaf2666. PubMed PMID: 29748285.

40. Eder K, Kalman B. Molecular heterogeneity of glioblastoma and its clinical relevance. Pathol Oncol Res. 2014;20(4):777-87. doi: 10.1007/s12253-014-9833-3. PubMed PMID: 25156108.

41. Zhou D, Wan Y, Xie D, Wang Y, Wei J, Yan Q, Lu P, Mo L, Xie J, Yang S, Qi X. DNMT1 mediates chemosensitivity by reducing methylation of miRNA-20a promoter in glioma cells. Exp Mol Med. 2015;47:e182. doi: 10.1038/emm.2015.57. PubMed PMID: 26337869; PMCID: PMC4650929.

42. Strauss J, Figg WD. Using Epigenetic Therapy to Overcome Chemotherapy Resistance. Anticancer Res. 2016;36(1):1-4. PubMed PMID: 26722021.

43. Li J, Hao D, Wang L, Wang H, Wang Y, Zhao Z, Li P, Deng C, Di LJ. Epigenetic targeting drugs potentiate chemotherapeutic effects in solid tumor therapy. Sci Rep. 2017;7(1):4035. doi: 10.1038/s41598-017-04406-0. PubMed PMID: 28642588; PMCID: PMC5481380.

44. Entin-Meer M, Yang X, VandenBerg SR, Lamborn KR, Nudelman A, Rephaeli A, Haas-Kogan DA. In vivo efficacy of a novel histone deacetylase inhibitor in combination with radiation for the treatment of gliomas. Neuro Oncol. 2007;9(2):82-8. doi: 10.1215/15228517-2006-032. PubMed PMID: 17347490; PMCID: PMC1871664.

45. Murai J, Huang SY, Das BB, Renaud A, Zhang Y, Doroshow JH, Ji J, Takeda S, Pommier Y. Trapping of PARP1 and PARP2 by Clinical PARP Inhibitors. Cancer Res. 2012;72(21):5588-99. doi: 10.1158/0008-5472.CAN-12-2753. PubMed PMID: 23118055; PMCID: PMC3528345.

46. Lord CJ, Ashworth A. PARP inhibitors: Synthetic lethality in the clinic. Science. 2017;355(6330):1152-8. doi: 10.1126/science.aam7344. PubMed PMID: 28302823; PMCID: PMC6175050.

47. Kedar PS, Stefanick DF, Horton JK, Wilson SH. Increased PARP-1 association with DNA in alkylation damaged, PARP-inhibited mouse fibroblasts. Mol Cancer Res. 2012;10(3):360-8. doi: 10.1158/1541-7786.MCR-11-0477. PubMed PMID: 22246237; PMCID: PMC3307909.

48. Berenguer-Daize C, Astorgues-Xerri L, Odore E, Cayol M, Cvitkovic E, Noel K, Bekradda M, MacKenzie S, Rezai K, Lokiec F, Riveiro ME, Ouafik L. OTX015 (MK-8628), a novel BET inhibitor, displays in vitro and in vivo antitumor effects alone and in combination with conventional therapies in glioblastoma models. International journal of cancer Journal international du cancer. 2016;139(9):2047-55. doi: 10.1002/ijc.30256. PubMed PMID: 27388964.

49. Karayan-Tapon L, Quillien V, Guilhot J, Wager M, Fromont G, Saikali S, Etcheverry A, Hamlat A, Loussouarn D, Campion L, Campone M, Vallette FM, Gratas-Rabbia-Re C. Prognostic value of O6-methylguanine-DNA methyltransferase status in glioblastoma patients, assessed by five different methods. J Neurooncol. 2010;97(3):311-22. doi: 10.1007/s11060-009-0031-1. PubMed PMID: 19841865.

50. Hegi ME, Diserens AC, Gorlia T, Hamou MF, de Tribolet N, Weller M, Kros JM, Hainfellner JA, Mason W, Mariani L, Bromberg JE, Hau P, Mirimanoff RO, Cairncross JG, Janzer RC, Stupp R. MGMT gene silencing and benefit from temozolomide in glioblastoma. N Engl J Med. 2005;352(10):997-1003. doi: 10.1056/NEJMoa043331. PubMed PMID: 15758010.

51. Lucio-Eterovic AK, Cortez MA, Valera ET, Motta FJ, Queiroz RG, Machado HR, Carlotti CG, Jr., Neder L, Scrideli CA, Tone LG. Differential expression of 12 histone deacetylase (HDAC) genes in astrocytomas and normal brain tissue: class II and IV are hypoexpressed in glioblastomas. BMC Cancer. 2008;8:243. doi: 10.1186/1471-2407-8-243. PubMed PMID: 18713462; PMCID: PMC2536671.

52. Zee BM, Levin RS, Xu B, LeRoy G, Wingreen NS, Garcia BA. In vivo residue-specific histone methylation dynamics. J Biol Chem. 2010;285(5):3341-50. doi: 10.1074/jbc.M109.063784. PubMed PMID: 19940157; PMCID: PMC2823435.

53. Breinig M, Klein FA, Huber W, Boutros M. A chemical-genetic interaction map of small molecules using high-throughput imaging in cancer cells. Mol Syst Biol. 2015;11(12):846. doi: 10.15252/msb.20156400. PubMed PMID: 26700849; PMCID: PMC4704494.

54. Oppermann S, Ylanko J, Shi Y, Hariharan S, Oakes CC, Brauer PM, Zuniga-Pflucker JC, Leber B, Spaner DE, Andrews DW. High-content screening identifies kinase inhibitors that overcome venetoclax resistance in

activated CLL cells. Blood. 2016;128(7):934-47. doi: 10.1182/blood-2015-12-687814. PubMed PMID: 27297795; PMCID: PMC5000578.

55. Pastori C, Daniel M, Penas C, Volmar CH, Johnstone AL, Brothers SP, Graham RM, Allen B, Sarkaria JN, Komotar RJ, Wahlestedt C, Ayad NG. BET bromodomain proteins are required for glioblastoma cell proliferation. Epigenetics. 2014;9(4):611-20. doi: 10.4161/epi.27906. PubMed PMID: 24496381; PMCID: PMC4121371.

56. Wadhwa E, Nicolaides T. Bromodomain Inhibitor Review: Bromodomain and Extra-terminal Family Protein Inhibitors as a Potential New Therapy in Central Nervous System Tumors. Cureus. 2016;8(5):e620. doi: 10.7759/cureus.620. PubMed PMID: 27382528; PMCID: PMC4917374.

57. Xu L, Chen Y, Mayakonda A, Koh L, Chong YK, Buckley DL, Sandanaraj E, Lim SW, Lin RY, Ke XY, Huang ML, Chen J, Sun W, Wang LZ, Goh BC, Dinh HQ, Kappei D, Winter GE, Ding LW, Ang BT, Berman BP, Bradner JE, Tang C, Koeffler HP. Targetable BET proteins- and E2F1-dependent transcriptional program maintains the malignancy of glioblastoma. Proc Natl Acad Sci U S A. 2018;115(22):E5086-E95. doi: 10.1073/pnas.1712363115. PubMed PMID: 29764999; PMCID: PMC5984485.

58. Ishida CT, Bianchetti E, Shu C, Halatsch ME, Westhoff MA, Karpel-Massler G, Siegelin MD. BH3-mimetics and BET-inhibitors elicit enhanced lethality in malignant glioma. Oncotarget. 2017;8(18):29558-73. doi: 10.18632/oncotarget.16365. PubMed PMID: 28418907; PMCID: PMC5444687.

59. Cheng Z, Gong Y, Ma Y, Lu K, Lu X, Pierce LA, Thompson RC, Muller S, Knapp S, Wang J. Inhibition of BET bromodomain targets genetically diverse glioblastoma. Clin Cancer Res. 2013;19(7):1748-59. doi: 10.1158/1078-0432.CCR-12-3066. PubMed PMID: 23403638; PMCID: PMC4172367.

60. Hottinger AF, Sanson M, Moyal E, Delord J-P, Micheli RD, Rezai K, Leung ACF, Perez S, Bekradda M, Lachaux N, Lokiec FM, Chinot OL. Dose optimization of MK-8628 (OTX015), a small molecule inhibitor of bromodomain and extra-terminal (BET) proteins, in patients (pts) with recurrent glioblastoma (GB). Journal of Clinical Oncology. 2016;34(15_suppl):e14123-e. doi: 10.1200/JCO.2016.34.15_suppl.e14123.

61. Ramadoss M, Mahadevan V. Targeting the cancer epigenome: synergistic therapy with bromodomain inhibitors. Drug Discov Today. 2018;23(1):76-89. doi: 10.1016/j.drudis.2017.09.011. PubMed PMID: 28943305.

62. Heinemann A, Cullinane C, De Paoli-Iseppi R, Wilmott JS, Gunatilake D, Madore J, Strbenac D, Yang JY, Gowrishankar K, Tiffen JC, Prinjha RK, Smithers N, McArthur GA, Hersey P, Gallagher SJ. Combining BET and HDAC inhibitors synergistically induces apoptosis of melanoma and suppresses AKT and YAP signaling. Oncotarget. 2015;6(25):21507-21. doi: 10.18632/oncotarget.4242. PubMed PMID: 26087189; PMCID: PMC4673282.

63. Bhadury J, Nilsson LM, Muralidharan SV, Green LC, Li Z, Gesner EM, Hansen HC, Keller UB, McLure KG, Nilsson JA. BET and HDAC inhibitors induce similar genes and biological effects and synergize to kill in Myc-induced murine lymphoma. Proc Natl Acad Sci U S A. 2014;111(26):E2721-30. doi: 10.1073/pnas.1406722111. PubMed PMID: 24979794; PMCID: PMC4084424.

64. Chen X, Zhang M, Gan H, Wang H, Lee JH, Fang D, Kitange GJ, He L, Hu Z, Parney IF, Meyer FB, Giannini C, Sarkaria JN, Zhang Z. A novel enhancer regulates MGMT expression and promotes temozolomide resistance in glioblastoma. Nat Commun. 2018;9(1):2949. doi: 10.1038/s41467-018-05373-4. PubMed PMID: 30054476; PMCID: PMC6063898.

65. Sengupta D, Kannan A, Kern M, Moreno MA, Vural E, Stack B, Jr., Suen JY, Tackett AJ, Gao L. Disruption of BRD4 at H3K27Ac-enriched enhancer region correlates with decreased c-Myc expression in Merkel cell carcinoma. Epigenetics. 2015;10(6):460-6. doi: 10.1080/15592294.2015.1034416. PubMed PMID: 25941994; PMCID: PMC4622756.

66. Loven J, Hoke HA, Lin CY, Lau A, Orlando DA, Vakoc CR, Bradner JE, Lee TI, Young RA. Selective inhibition of tumor oncogenes by disruption of super-enhancers. Cell. 2013;153(2):320-34. Epub 2013/04/16. doi: 10.1016/j.cell.2013.03.036. PubMed PMID: 23582323; PMCID: 3760967.

67. Quinn JA, Jiang SX, Reardon DA, Desjardins A, Vredenburgh JJ, Gururangan S, Sampson JH, McLendon RE, Herndon JE, 2nd, Friedman HS. Phase 1 trial of temozolomide plus irinotecan plus O6-benzylguanine in adults with recurrent malignant glioma. Cancer. 2009;115(13):2964-70. doi: 10.1002/cncr.24336. PubMed PMID: 19402172; PMCID: PMC2748258.

68. Quinn JA, Jiang SX, Reardon DA, Desjardins A, Vredenburgh JJ, Rich JN, Gururangan S, Friedman AH, Bigner DD, Sampson JH, McLendon RE, Herndon JE, Jr., Walker A, Friedman HS. Phase I trial of temozolomide plus O6-benzylguanine 5-day regimen with recurrent malignant glioma. Neuro Oncol. 2009;11(5):556-61. doi: 10.1215/15228517-2009-007. PubMed PMID: 19289491; PMCID: PMC2765345.

69. Quinn JA, Jiang SX, Reardon DA, Desjardins A, Vredenburgh JJ, Rich JN, Gururangan S, Friedman AH, Bigner DD, Sampson JH, McLendon RE, Herndon JE, 2nd, Walker A, Friedman HS. Phase II trial of temozolomide plus o6-benzylguanine in adults with recurrent, temozolomide-resistant malignant glioma. J Clin Oncol. 2009;27(8):1262-7. doi: 10.1200/JCO.2008.18.8417. PubMed PMID: 19204199; PMCID: PMC2667825.